



Adakitic (tonalitic-trondhjemite) magmas resulting from eclogite decompression and dehydration melting during exhumation in response to continental collision

Shuguang Song ^{a,*}, Yaoling Niu ^{b,c}, Li Su ^d, Chunjing Wei ^a, Lifei Zhang ^a

^a MOE Key Laboratory of Orogenic Belts and Crustal Evolution, School of Earth and Space Sciences, Peking University, Beijing 100871, China

^b Department of Earth Sciences, Durham University, Durham DH1 3LE, UK

^c Institute of Oceanology, Chinese Academy of Science, Qingdao 266071, China

^d Institute of Earth Sciences, Chinese University of Geosciences, Beijing 100083, China

Received 22 April 2013; accepted in revised form 9 January 2014; Available online 18 January 2014

Abstract

Modern adakite or adakitic rocks are thought to result from partial melting of younger and thus warmer subducting ocean crust in subduction zones, with the melt interacting with or without mantle wedge peridotite during ascent, or from melting of thickened mafic lower crust. Here we show that adakitic (tonalitic-trondhjemite) melts can also be produced by eclogite decompression during exhumation of subducted and metamorphosed oceanic/continental crust in response to continental collision, as exemplified by the adakitic rocks genetically associated with the early Paleozoic North Qaidam ultra-high pressure metamorphic (UHPM) belt on the northern margin of the Greater Tibetan Plateau. We present field evidence for partial melting of eclogite and its products, including adakitic melt, volumetrically significant plutons evolved from the melt, cumulate rocks precipitated from the melt, and associated granulitic residues. This “adakitic assemblage” records a clear progression from eclogite decompression and heating to partial melting, to melt fractionation and ascent/percolation in response to exhumation of the UHPM package. The garnetite and garnet-rich layers in the adakitic assemblage are of cumulate origin from the adakitic melt at high pressure, and accommodate much of the Nb–Ta–Ti. Zircon SHRIMP U–Pb dating shows that partial melting of the eclogite took place at ~435–410 Ma, which postdates the seafloor subduction (>440 Ma) and temporally overlaps the UHPM (~440–425 Ma). While the geological context and the timing of adakite melt formation we observe differ from the prevailing models, our observations and documentations demonstrate that eclogite melting during UHPM exhumation may be important in contributing to crustal growth.

© 2014 Elsevier Ltd. All rights reserved.

1. INTRODUCTION

Sodium-rich tonalitic-trondhjemite rock suites play an important role in the growth of the continental crust growth throughout Earth's history (e.g. Martin et al., 2005). In modern volcanic arc environments, these rocks are generally referred to as “adakites” by their geochemical characteristics of high Sr, low HREE and thus high Sr/Y and La/Yb ratios, and are thought to be produced by

melting of “slabs” of subducting ocean crust when it is relatively young (<25 Ma) and warm (e.g., Defant and Drummond, 1990; Schmidt and Poli, 1998; Rapp et al., 2003; Martin et al., 2005). While this interpretation is reasonable, alternative models have been proposed to explain these and other adakite magmas in geological histories and in settings that do not seem to be associated with active subduction (Atherton and Petford, 1993; Sajona et al., 1993; Peacock et al., 1994; Rudnick, 1995; Arculus et al., 1999; Castillo et al., 1999; Castillo, 2006, 2012; Gutscher et al., 2000; Yogodzinski et al., 2001; Beate et al., 2001; Xu et al., 2002; Chung et al., 2003; Macpherson et al.,

* Corresponding author. Tel.: +86 10 62767729.
E-mail address: sg.song@pku.edu.cn (S. Song).

2006). As summarized by Castillo (2012), investigation of adakite has been important in our understanding of (1) metasomatism of the mantle wedge and processes related to the general issue of crustal recycling, and (2) Archaean trondjemite-tonalite-granodiorite (TTG) formation and crustal evolution. Geochemical and experimental data suggest that adakite is formed by partial melting of basaltic rocks under conditions where garnet, rutile and amphibole are present as residual phases (Defant and Drummond, 1990; Foley et al., 2002; Rapp et al., 2003; Xiong et al., 2005; Xiong, 2006), but whether subducting oceanic crust under eclogite facies conditions can melt or not within the subduction channel remains debatable (see Garrison and Davidson, 2003; Dreher et al., 2005; Macpherson et al., 2006; Castillo, 2006, 2012).

Ultrahigh-pressure (UHP) metamorphic belts within continental orogens have witnessed orogenic processes from seafloor subduction to continental crust subduction and exhumation (e.g., Ernst, 2001; Chopin, 2003; Song et al., 2006). Magmatism associated with these processes has been reported in several UHPM belts, e.g., the Kokchetav massif (Hermann et al., 2001; Parkinson and Kohn, 2002; Korsakov and Hermann, 2006; Kotkova and Harley, 2010), the Western Gneiss Region (Labrousse et al., 2004, 2011; Lang and Gilotti, 2007), the Dabie-Sulu (Wallis et al., 2005; Zhao et al., 2012; Xu et al., 2013), and the North Qaidam and Qilian (Song et al., 2009, 2012; Chen et al., 2012; Yu et al., 2012). Most of the studies focused on leucosomes or leocgranites that are interpreted to result from decompression melting of the felsic crust during continental exhumation (e.g. Hermann and Spandler, 2008; Labrousse et al., 2011). Decompression melting of felsic rock at the eclogite/amphibolite facies transition during retrogression has been studied experimentally (Auzanneau et al., 2006). Archean tonalitic melts are interpreted to have formed as a result of amphibole dehydration under medium-pressure granulite-facies conditions (Nehring et al., 2009). Melting of eclogites at eclogite/granulite facies transition in Phanerozoic HP–UHP metamorphic terranes, however, has not been well investigated although some syn- or post-collisional adakitic rocks have been reported in recent years (e.g., Zeng et al., 2011; Labrousse et al., 2011; Topuz et al., 2011). Adakitic melts were first reported in the North Qaidam UHPM belt by Song et al. (2009). Yu et al. (2012) carried out a study on some adakitic melts and suggested that they were the result of melting of thickened lower crust.

In this paper, we report field, petrologic and geochemical observations to show that adakite magmas can be produced through decompression melting of eclogite during exhumation of combined UHP-metamorphosed oceanic and continental crust, in response to continental collision, as recorded in the North Qaidam ultra-high pressure metamorphic (UHPM) belt at the northern margin of the Greater Tibetan Plateau. Both the melting process and high-pressure crystallization contribute to the observed adakitic magmas.

2. REGIONAL GEOLOGY AND PETROGRAPHY

The North Qaidam UHPM belt marks the Early Paleozoic continental-type subduction and exhumation between

the Qaidam block and Qilian block (Fig. 1). This belt is dominated by Grenville-age granitic gneisses with blocks of eclogite, pelitic gneiss/schist and garnet peridotite (see in details in the review paper by Song et al., 2014). The study area in the Dulan UHPM terrane is located at the eastern end of the North Qaidam UHPM belt and has been subdivided into the North Dulan belt (NDB) and the South Dulan belt (SDB) (Fig. 1; Song et al., 2003b).

The protoliths of the NDB eclogite are dominated by fragmented ~500–550 Ma ophiolite (basalts, gabbros and harzburgite) and ~830–850 Ma continental flood basalts metamorphosed at conditions of $P = 2.9\text{--}3.3 \text{ GPa}$ and $T = 630\text{--}730 \text{ }^{\circ}\text{C}$ (Song et al., 2003a,b, 2006, 2010; Yang et al., 2006; Zhang et al., 2008; Zhang et al., 2010). Zircon SHRIMP dating from eclogites yielded two stages of 440–460 Ma and 422–440 Ma (Song et al., 2006; Mattinson et al., 2006, 2009; Zhang et al., 2008, 2010), whereas coesite-bearing zircons from the paragneisses and eclogite gave UHP metamorphic ages of 438–423 Ma (Song et al., 2006; Zhang et al., 2010).

In the SDB, three lithological units can be subdivided from north to south: (1) granitic gneisses with eclogite blocks, the same as those in the NBD; (2) mafic granulite (granulitized eclogite) + tonalitic-trondjemitic melts, and (3) a tonalite pluton. The mafic granulites are retrogressed from eclogites with strong overprint of high-pressure (HP) granulite facies assemblages stable at conditions of $P = 1.86\text{--}2.0 \text{ GPa}$ and $T = 873\text{--}948 \text{ }^{\circ}\text{C}$ (Song et al., 2003b). Some felsic melts are also uniformly distributed in the matrix of the granulitized eclogite (Fig. 2a).

2.1. Mafic granulite

The mafic granulite occurs as irregular-shaped blocks of various sizes (10 cm to 1–2 m) within tonalite-dominated melts. The mineralogy of mafic granulite blocks consists of garnet + clinopyroxene (cpx, $\text{Jd} < 20 \text{ mol\%}$) (Fig. 2b) with varying amounts of plagioclase, rutile, kyanite and scapolite. Garnet is coarse-grained euhedral crystals and characterized by high MgO (7.5–8.9 wt%), CaO (8.8–10.5 wt%) and low FeO (17–22 wt%) (e.g., pyrope, 25–32.5 mol%; grossular, 23–29.5 mol%; almandine, 37.5–43.6 mol%), different from garnets in eclogite (Song et al., 2003b) and from garnet in garnetite (Fig. 3). The earlier omphacite ($\text{Jd}_{45\text{--}48}$) is retained as inclusions in kyanite (Fig. 2c), suggesting that the HP granulite facies metamorphism overprints the former eclogite. Symplectites of former eclogitic garnet and omphacite are well-developed. The sodic plagioclase ($\text{Ab}_{75\text{--}92}$) occurs as irregular-shaped segregations between symplectites of cpx and garnet; the euhedral zircon and needle-like apatite crystals in these segregations suggest they represent melt pockets extracted from the breakdown of omphacite (and garnet) during decompression from eclogite to HP granulite (Fig. 2d and e).

2.2. Garnetite and tonalitic-trondjemitic melts

Tonalitic-trondjemitic melts in the middle part of the section occur as layers or veinlets mixed together with the irregular-shaped mafic granulite blocks (Fig. 2f–h). Three

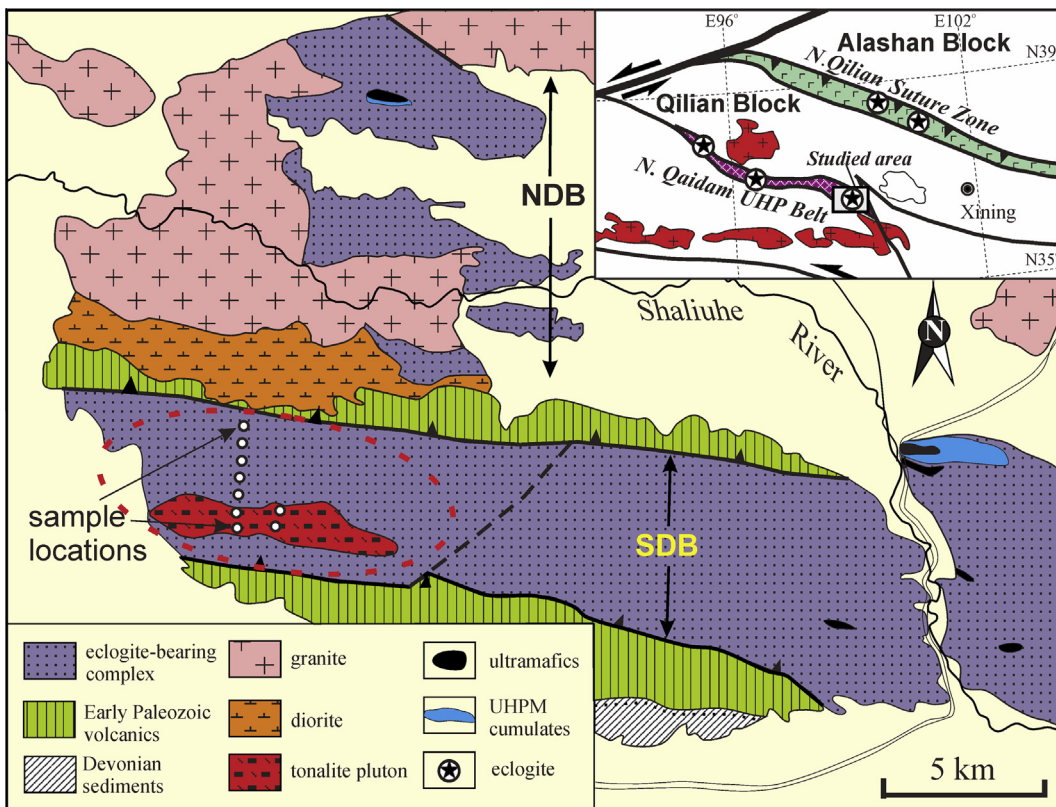


Fig. 1. Geological map of the Dulan UHPM terrane showing sample locations (Modified after Song et al., 2003b and Zhang et al., 2010).

lithologies are apparent in the field: (1) garnetite, (2) garnet-bearing tonalite, and (3) garnet-free trondhjemite. The tonalite pluton ($\sim 1.5 \times 7$ km across) in the south (Fig. 1) is compositionally rather uniform with no mafic enclaves (also see below).

The garnetite (GA) occurs as 5–30 cm thick layers interbedded conformably with garnet-bearing tonalite/trondhjemite layers (GT; Fig. 2f). It consists of ~90 vol% of euhedral garnet and shows a typical cumulate texture with intercumulus plagioclase + rutile + sphene + allanite + minor zircon (Fig. 2i). All the garnet crystals contain abundant inclusions/exsolutions of rutile + apatite + monazite needles (Fig. 2i); some grains show oscillatory zoning with rutile needles and albite crystallizing along hexagonal crystallographic planes (Fig. 2j), similar to igneous garnets reported by Clarke et al. (2013). Comparing to garnet in granulites, garnet in garnetite has high CaO (11.8–12.6 wt%), TiO₂ (0.21–0.63 wt%), FeO (22.5–25.3 wt%) and low MgO (5–5.7 wt%) with pyrope (18.3–20.7 mol%), grossular (31.4–34.1 mol%), Almandine (46–53 mol%). The crystal features, together with its distinctive composition, indicate that the garnet crystals must have precipitated from high-Ti melts at high pressures. The plagioclases in the garnetite are albite and oligoclase with Ab contents ranging from 96 to 80 mol%, also suggesting high-pressure accumulation.

The garnet-bearing tonalite is the major component of the tonalite-trondhjemite melts in the middle part of the section and contains irregularly shaped granulite blocks (Fig. 2g and h). Some occur as layers conformably

with HP granulite and garnetite (Fig. 2f). Minerals in the garnet-bearing tonalite are high-pressure assemblages of garnet + kyanite + plagioclase + quartz + rutile + allanite, and garnet + cpx + plagioclase + quartz + rutile + allanite. These garnet crystals, as in garnet in the garnetite, are rich in CaO and TiO₂ and have densely-packed needle-like rutile and apatite inclusions. Cpx has high contents of Al₂O₃ (8.3–8.7 wt%) and Na₂O (2.7–3.0 wt%) with jadeite content of 14–21 mol% and most crystals have been retrograded to amphibole + plagioclase (Fig. 2k). Allanite can be as much as ~2–3 vol% in some samples (Fig. 2k), and all grains show clear oscillatory growth bands, suggesting their crystallization from a LREE-rich melt (Fig. 2l). *P-T* calculation using Grt-Cpx-Pl-Qtz geothermobarometers (Ellis and Green, 1979; Powell, 1985; Eckert et al., 1991) yield *P* = 18.5–19.6 kbar and *T* = 908–930 °C, which may represent the *P-T* conditions of crystallization of the garnet-tonalite and garnetite. The garnet-free felsic layers (trondhjemite) consist of oligoclase + quartz with minor amphibole + allanite + rutile; some occur as irregular veins cutting the mafic granulite (Fig. 2h).

2.3. Tonalite pluton

The tonalite pluton (Fig. 1) is an elongated, irregular-shaped body of ~1–2 km wide and ~7 km long. It intrudes amphibolite-facies metamorphic country rocks with clear, fine-grained chilled margins. The lithology of the pluton is fairly homogenous and consists of a mineral assemblage of oligoclase + amphibole + quartz plus minor allanite,

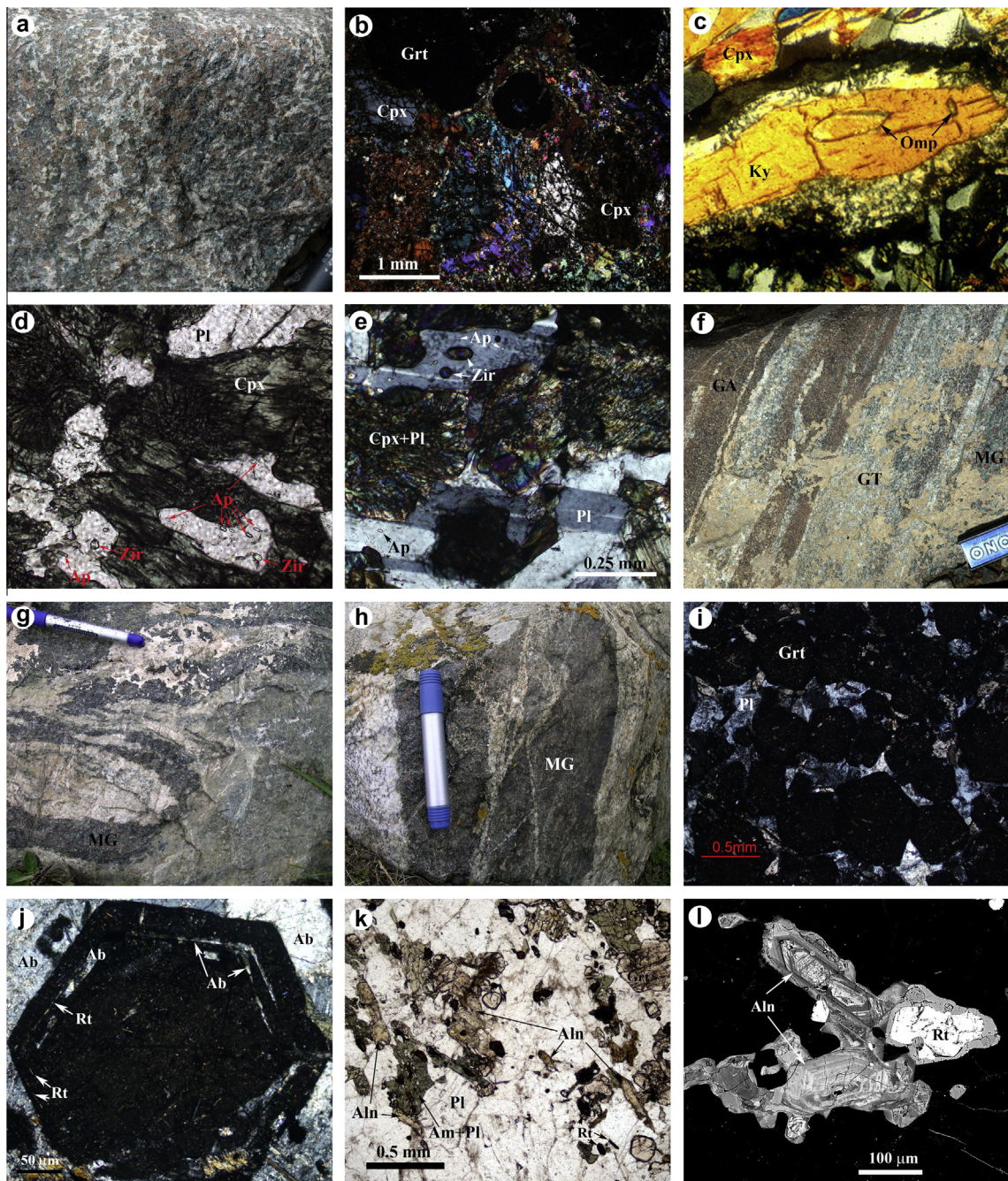


Fig. 2. Photographs of various rocks in the field and thin-sections. (a) Mafic granulite (MG) (granulitized eclogite) with felsic melt pockets extracting from decompression melting reaction of eclogite. (b) Mafic granulite showing bimimetic assemblage of garnet (Grt) + clinoxyroxene (Cpx) with rare rutile, which represents the residue after high-degree of melting. (c) Omphacite (Omp, Jd > 40 mol%) inclusions in kyanite (Ky). (d) and (e) Sodic plagioclase (Pl) melts generated by decompression of Cpx (symplectite Cpx + Pl). Note the newly-crystallized euhedral zircon (Zir) and apatite needles occur within the Pl melt pockets, suggesting magmatic origin. (f) Interlayers of cumulate garnetite (GA) and garnet-bearing tonalite (GT) with and relict mafic granulite (MG). (g) Irregular relic mafic granulite restile within garnet-bearing tonalite. (h) Residual mafic granulite block within garnet-free tonalite/trondhjemite. (i) Photomicrograph showing accumulated euhedral garnet (Grt) crystals from garnetite. Note that albite and sphene occur as intercumulus phases between the euhedral garnet and all garnets contain densely-packed rutile + apatite needles. (j) Euhedral garnet in garnetite showing oscillatory textures with rutile needles growing on crystallographic planes, indicating igneous origin. (k) Photomicrograph showing tonalite (DL52) with garnet (Grt), Cpx (retrograde into amphibole (Am) + Pl), allanite (Aln) and rutile (Rt). (l) Back-scattered image showing growth bands of allanite in tonalite, suggesting magmatic origin (DL52).

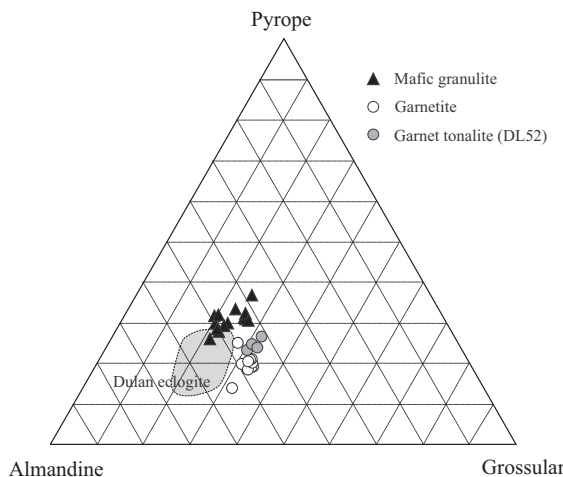


Fig. 3. Diagram showing compositional distinctions of garnet from mafic granulite, garnetite and Dulan eclogites.

ilmenite, apatite and zircon. No rutile has been found in samples from the pluton.

3. GEOCHEMISTRY

3.1. Methods

Bulk-rock major element oxides (SiO_2 , TiO_2 , Al_2O_3 , FeO , MnO , MgO , CaO , Na_2O , K_2O , and P_2O_5) were determined with a Leeman Prodigy inductively coupled plasma-optical emission spectroscopy (ICP-OES) system with high dispersion Echelle optics at China University of Geosciences, Beijing (CUGB). Precisions (1σ) for most elements based on US Geological Survey rock standards BCR-1, AGV-2 and GSR-3 plus Chinese national geological standard reference materials (SRM) are better than 1% with the exception of TiO_2 (~1.5%) and P_2O_5 (~2.0%). Loss on ignition (LOI) was determined by placing 1 g sample in the furnace at 1000 °C for several hours before cooling in a desiccator and re-weighing.

Whole-rock trace elements (Tables 1–3) were analyzed using an Agilent-7500a inductively coupled plasma mass spectrometry (ICP-MS) at CUGB. 50 mg sample was dissolved in equal mixture of subboiling-distilled pure HF and HNO_3 with a Teflon digesting vessel on a hot-plate for 24 h. This procedure was repeated using smaller amounts of acids for a further 12 h. After digestion, the sample was evaporated to incipient dryness, refluxed with 6 N HNO_3 , and heated again to incipient dryness. The sample was then dissolved in 2 mL of 3 N HNO_3 and diluted with Milli-Q water (18 mega-ohm) to a final total dissolved solid of 0.05%. Two USGS rock reference materials BCR-1 and BHVO-1 were used to monitor the analytical accuracy and precision. Analytical accuracy, as indicated by relative difference (RE) between measured and recommended values is better than 10% for most elements, ranging between 10% and 13% for Cu, Sc, Nb, Er, Th, and U, and between 11% and 20% for Ta, Tm, and Gd.

Sr-Nd isotopic compositions of representative samples (Table 4) were determined using a MAT-262 mass

spectrometer in the Institute of Geology and Geophysics, CAS following Yang et al. (2010). The ${}^{87}\text{Sr}/{}^{86}\text{Sr}$ ratios were normalized against ${}^{86}\text{Sr}/{}^{88}\text{Sr} = 0.1194$. All ratios have been adjusted against Sr standard NBS-987 $\text{Sr} = 0.710250$. Measured ${}^{143}\text{Nd}/{}^{144}\text{Nd}$ ratios were normalized to ${}^{146}\text{Nd}/{}^{144}\text{Nd} = 0.7219$, and the reported ${}^{143}\text{Nd}/{}^{144}\text{Nd}$ ratios were further adjusted relative to the Shin Etsu JNDI-1 standard of 0.512115. Initial ${}^{143}\text{Nd}/{}^{144}\text{Nd}$ ratios and corresponding $\varepsilon_{\text{Nd}}(t)$ values were calculated on the basis of present-day reference values for CHUR: $({}^{143}\text{Nd}/{}^{144}\text{Nd})_{\text{CHUR}} = 0.512638$ and $({}^{147}\text{Sm}/{}^{144}\text{Nd})_{\text{CHUR}} = 0.1967$.

3.2. Results and interpretation

Representative whole-rock analyses of the HP mafic granulite (granulitized eclogite) blocks, garnetite, tonalitic-trondhjemite melts and the tonalite pluton are given in Tables 1–3. All these samples are characterized as low- to medium-K (Fig. 4), and the chemical composition varies considerably among the four rock-types.

3.2.1. Major and trace elements

The mafic granulites have low SiO_2 (41.6–47.4 wt%), TiO_2 (0.22–0.81 wt%), K_2O (0.06–0.37 wt%), and high Al_2O_3 (15.5–22.1 wt%) with varying $\text{Mg}^{\#}$ (0.40–0.69) that is inversely correlated with TiO_2 and REE abundances. They also have overall low abundances of incompatible elements (those more incompatible than Sm) with relatively low $[\text{La}/\text{Sm}]_{\text{N}} = \sim 1.75$, $[\text{Sm}/\text{Yb}]_{\text{N}} = \sim 2.46$ and $[\text{La}/\text{Yb}]_{\text{N}} = \sim 4.52$. Their strong depletion of Nb-Ta relative to La (Fig. 5a), large sub-chondritic variation of Nb/Ta (1.2–16.5) and its significant positive correlations with LREEs, Nb, Y, P and other incompatible elements is consistent with Nb being more incompatible than Ta during melting (Niu, 2004). The strong Zr-Hf depletion relative to Sm along with subchondritic Zr/Hf (16.9–33.7) ratios is also consistent with Zr being more incompatible than Hf expected for melting residues (Niu, 2004). All these observations corroborate the interpretation that the mafic granulites are the melting residues of the UHPM eclogite for the coexisting tonalitic and trondhjemite melts (see below). The essentially identical trace element patterns yet slightly different abundance levels are also consistent with the mafic granulite being the melting residues with varying amounts of the trapped “adakitic melt”, similar to some Archean granulite residue in TTG gneisses (e.g., Nehring et al., 2009).

The garnetite samples have low SiO_2 (39.6–48.1 wt%), K_2O (0.17–0.79 wt%), and high TiO_2 (1.96–3.31 wt%), Al_2O_3 (18.6–19.3 wt%) and P_2O_5 (0.56–0.75 wt%). They also have overall high abundances of incompatible elements (including LILEs and HFSEs), much higher than those in the mafic granulites and the adakitic melts. The low, *not high*, HREE feature suggests that the garnetites are of cumulate origin and the garnets were precipitated from a Ti-rich, HREE-depleted (adakitic) melts (Fig. 5b).

The tonalitic-trondhjemite melts display a large compositional variation in terms of major elements (SiO_2 57.5–73.3 wt%, TiO_2 0.1–1.84 wt%, $\text{Mg}^{\#}$ 0.43–0.72), trace elements ($\text{Sr} = 482$ –1862 ppm), and key elemental ratios

Table 1

Whole-rock major (wt%) and trace element (ppm) abundances of tonalite/trondhjemite melts and granitite cumulate.

Sample	DL-25 Ton	DL-36a Trond	DL-37 Trond	DL-44 G-Ton	DL-52 G-Ton	DL-58 Ton	Q115 G-Ton	Q116 Trod	Q122 G-Ton	Q123 G-Ton	Q126 Ton	DL-106 Trond	DL-109 Trond	DL-110 Trond	DL-23a GT	DL-23b GT	DL-26 GT
SiO ₂	65.16	73.29	70.81	66.18	57.49	63.03	68.51	69.83	67.41	68.67	68.86	67.36	69.66	68.91	39.87	41.42	48.06
TiO ₂	0.97	0.23	0.12	0.10	1.84	0.30	0.19	0.19	0.24	0.56	0.23	0.17	0.21	0.20	3.31	3.23	1.96
Al ₂ O ₃	16.96	13.56	16.44	15.75	20.40	16.71	16.94	16.19	18.13	17.90	17.69	17.55	15.64	15.97	18.82	18.59	19.53
Fe ₂ O ₃ T	2.47	0.96	1.36	2.39	2.51	4.81	2.70	2.21	2.07	2.37	2.28	1.74	1.83	1.52	19.54	15.92	12.07
MnO	0.03	0.02	0.03	0.03	0.02	0.09	0.09	0.06	0.04	0.05	0.04	0.04	0.03	0.02	0.15	0.12	0.14
MgO	1.89	1.26	0.79	0.74	1.60	2.12	1.05	0.87	1.30	0.97	1.14	0.89	1.12	1.09	4.43	4.02	5.41
CaO	3.58	1.61	3.18	10.95	6.95	7.41	4.56	4.11	3.65	3.89	5.56	4.76	2.95	2.04	12.17	11.99	7.85
Na ₂ O	5.84	5.57	4.11	1.82	6.79	3.60	4.31	4.59	4.88	3.72	2.35	4.95	5.77	7.29	1.36	2.40	3.06
K ₂ O	0.64	1.18	1.09	0.37	0.66	0.59	0.24	0.64	0.72	0.98	0.89	0.73	1.30	0.61	0.17	0.27	0.79
P ₂ O ₅	0.27	0.13	0.07	0.05	0.42	0.05	0.15	0.13	0.08	0.08	0.09	0.03	0.04	0.07	0.75	0.68	0.56
LOI	1.64	1.51	1.44	0.96	0.64	1.05	0.72	1.08	1.67	1.03	0.88	1.21	1.74	1.53	-0.05	1.39	1.25
Total	99.45	99.30	99.44	98.91	99.31	99.75	99.47	99.89	100.20	99.92	100.01	99.40	100.24	99.26	100.35	100.04	100.69
Mg#	0.601	0.722	0.533	0.379	0.558	0.467	0.435	0.439	0.555	0.448	0.497	0.504	0.549	0.586	0.310	0.370	0.511
Sc	4.338	1.398	2.396	7.158	5.102	14.022	6.492	4.899	6.409	5.085	3.217	3.310	3.448	3.720	10.674	9.122	17.720
V	71.48	36.98	20.12	102.80	151.48	121.10	54.11	58.90	55.27	45.51	34.01	24.20	22.24	25.18	110.98	126.90	147.68
Cr	16.458	14.370	10.572	23.860	15.164	8.506	1.711	2.186	3.691	2.218	2.458	18.520	34.240	27.780	13.750	11.982	46.040
Co	16.008	18.480	18.416	20.860	18.112	18.918	6.449	5.201	5.257	4.494	4.316	14.106	21.240	14.212	37.600	27.200	22.000
Ni	4.798	2.708	2.102	4.298	6.892	3.222	0.925	0.869	2.644	1.775	1.858	5.954	15.104	13.138	5.938	12.252	15.934
Cu	12.814	10.218	4.694	12.686	19.990	3.364	9.308	13.060	25.270	4.580	5.148	7.094	26.220	28.240	45.980	87.420	30.980
Zn	80.84	21.36	31.80	15.16	47.14	47.90	39.85	20.02	34.85	19.62	26.89	35.96	41.94	38.66	123.24	101.06	86.44
Ga	18.414	14.016	11.118	19.046	25.220	14.026	15.590	18.450	20.510	29.150	22.940	14.390	17.882	18.498	20.640	21.240	19.600
Rb	26.920	46.200	98.080	15.540	7.894	19.246	3.192	25.920	92.010	96.520	38.750	16.374	44.160	24.260	5.216	5.196	31.840
Sr	1036.4	667.80	768.80	1337.4	1863.8	1109.6	751.40	758.30	984.20	746.30	920.50	1253.6	510.80	482.40	317.20	500.60	697.40
Y	6.684	1.417	1.400	2.764	3.034	3.140	4.827	5.179	3.690	3.733	3.642	2.828	4.886	4.980	24.820	20.900	27.680
Zr	281.60	30.220	5.860	37.080	313.60	35.200	12.770	15.990	56.720	59.730	85.720	42.860	102.00	112.02	269.40	211.60	323.00
Nb	12.082	2.170	1.129	0.922	28.120	1.095	0.930	0.979	2.095	8.276	1.652	2.834	1.096	1.108	24.340	24.720	31.220
Cs	1.079	0.871	3.998	0.290	0.470	0.866	0.540	1.388	3.041	4.731	1.577	0.974	1.029	1.380	0.185	0.164	1.292
Ba	187.78	298.60	583.00	95.420	208.40	162.18	70.590	119.40	168.90	359.00	203.70	1635.2	343.40	219.20	29.280	33.020	161.40
La	41.080	35.540	1.344	4.680	86.480	2.284	7.471	10.970	4.758	6.162	16.710	3.484	8.632	7.700	83.140	87.020	44.580
Ce	87.240	71.260	2.528	8.398	164.78	4.352	15.810	23.080	9.592	12.980	36.440	7.052	17.940	16.710	233.80	248.80	100.62
Pr	9.546	7.802	0.328	1.097	17.562	0.600	1.949	2.827	1.200	1.609	4.054	0.827	2.134	2.056	31.240	32.880	11.170
Nd	33.720	28.260	1.274	4.052	60.760	2.858	7.646	10.900	4.845	6.146	15.070	3.068	8.732	8.468	128.86	133.08	42.800
Sm	5.024	4.274	0.262	0.923	8.022	0.633	1.301	1.817	0.942	1.117	2.268	0.601	1.863	1.875	27.080	25.640	9.402
Eu	1.092	0.588	0.216	0.386	1.491	0.369	0.454	0.645	0.394	0.478	0.699	0.340	0.599	0.596	6.200	5.886	2.452
Gd	3.134	1.948	0.228	0.670	3.898	0.631	1.093	1.435	0.842	0.944	1.547	0.536	1.568	1.673	20.500	18.812	10.456
Tb	0.332	0.147	0.033	0.090	0.304	0.092	0.141	0.181	0.111	0.129	0.158	0.076	0.201	0.203	2.174	1.874	1.365
Dy	1.549	0.464	0.206	0.568	0.984	0.592	0.883	1.040	0.689	0.777	0.763	0.490	1.024	1.064	8.002	6.746	6.562
Ho	0.248	0.056	0.047	0.107	0.113	0.123	0.175	0.194	0.142	0.146	0.146	0.099	0.177	0.181	0.890	0.717	0.957
Er	0.620	0.116	0.150	0.319	0.235	0.374	0.497	0.544	0.405	0.379	0.396	0.328	0.482	0.483	1.594	1.282	2.256
Tm	0.077	0.012	0.023	0.042	0.023	0.056	0.075	0.075	0.059	0.055	0.058	0.050	0.064	0.065	0.153	0.115	0.276
Yb	0.452	0.066	0.167	0.272	0.115	0.373	0.523	0.528	0.360	0.356	0.387	0.361	0.408	0.432	0.758	0.543	1.679
Lu	0.061	0.008	0.029	0.040	0.015	0.065	0.083	0.085	0.055	0.059	0.061	0.061	0.059	0.062	0.096	0.061	0.238

Hf	5.130	0.770	0.178	1.082	6.186	0.865	0.351	0.430	1.367	1.578	2.415	1.433	2.802	3.064	4.990	4.478	6.378
Ta	1.108	0.149	0.067	0.114	2.262	0.218	0.084	0.079	0.124	1.255	0.109	0.194	0.096	0.102	3.364	2.244	2.392
Pb	9.510	7.168	10.268	24.180	13.584	11.052	2.253	2.444	7.896	16.830	4.502	16.328	4.450	4.136	2.454	3.444	5.598
Th	15.420	14.734	0.142	1.256	30.480	0.092	0.434	0.643	0.326	0.645	3.555	0.855	2.276	1.951	23.520	25.720	14.118
U	0.833	0.578	0.277	1.795	1.509	0.100	0.216	0.331	0.200	1.827	0.432	1.557	0.664	0.686	5.320	6.242	1.232

Ton = Tonalite; G-Ton = garnet tonalite; Trond = trondhjemite; GT = garnetite.

$[La/Sm]_N = 2.33\text{--}6.96$, $[Sm/Yb]_N = 1.85\text{--}77$; $[La/Yb]_N = 4.40\text{--}538$). The inverse correlation of Sr, Zr, La with SiO_2 (not shown) defined by garnet-bearing tonalite and the more evolved trondhjemite is consistent with advanced degrees of fractionation towards a SiO_2 -rich melt. The linear or curvilinear trends of major and trace elements with SiO_2 for garnetite, tonalitic-trondhjemitic melts and the tonalite pluton, as shown in Fig. 6, as well as their field and petrographic observations described above, reflect that these rocks have experienced varying extents of fractionation with varying modal mineralogical (mostly garnet- and plagioclase-controlled) accumulation at high pressures. Samples with low La/Yb and a high positive Eu^{*} anomaly reflects plagioclase accumulation, the two samples (07DL36 and 07DL52) with extremely high La/Yb ratios reflect allanite accumulation (Fig. 2k), and TiO_2 and P_2O_5 negatively linear trends with SiO_2 suggest that most rutile and apatite have precipitated together with garnet in the garnetite and garnet-rich tonalite at high pressures (1.8–2.0 GPa).

All tonalitic-trondhjemitic melts show variable subchondritic Nb/Ta ratios (Fig. 4c), which can be readily explained by Nb-Ta partitioning behaviors of consistently high $D_{solid/melt}$ for Ta relative to Nb during fractional crystallization (Green, 1995; Niu and Batiza, 1997). It is thus apparent that the characteristic depletion of Nb, Ta and Ti and superchondritic Nb/Ta ratios in the adakitic pluton with uniform compositions (Fig. 5d) are consequently in turn resulted from fractionation of garnet and rutile at high pressure.

Except for the garnetites (Fig. 5b), all the above melt assemblages are geochemically broadly similar to typical modern adakites (Fig. 5c,d, and Fig. 7), especially the lithologically uniform tonalite pluton (Fig. 5d with elevated $Sr \sim 608\text{--}1814$ ppm, $[La/Sm]_N = 4.98 \pm 0.56$, $[Sm/Yb]_N = 4.00 \pm 0.48$ and $[La/Yb]_N = 19.9 \pm 3.26$).

3.2.2. Sr–Nd isotopes

The Sr–Nd isotope data are given in Table 4 and shown in Fig. 8. The initial isotopic ratios were corrected to 420 Ma. All the samples (including mafic granulite, tonalite-trondhjemite melts and tonalite pluton) show a relatively narrow variation in Sr–Nd isotope space with I_{Sr} (420 Ma) = 0.7041–0.7075 and $\epsilon_{Nd}(T) = +0.13$ to +3.13, respectively, similar to Sr–Nd isotopic compositions of eclogites from the UHP-metamorphosed ophiolite (oceanic crust) in the north Dulan belt (Song et al., 2003a; Zhang et al., 2008). The decrease in initial ϵ_{Nd} radios from eclogite protolith to adakitic melts is consistent with the crustal contamination of the melt during ascent and intrusion.

4. ZIRCON GEOCHRONOLOGY AND HF ISOTOPE

Four representative samples were selected for zircon U, Th and Pb analysis using SHRIMP II at Beijing SHRIMP Centre, Chinese Academy of Geosciences, and LA-ICP-MS at China University of Geosciences in Beijing, following the analytical conditions and procedures of Song et al. (2005b, 2010). Results are shown in Tables 5 and 6 and Fig. 9. Zircon Hf isotope was analyzed using a Geolas-193

Table 2

Whole-rock major and trace element abundances of the tonalite pluton.

Sample	DL-29 Tonilite	DL-30 Tonilite	DL-38 Tonilite	DL-42 Tonilite	DL-47 Tonilite	DL-48 Tonilite	DL-51 Tonilite	DL-92 Tonilite	5Q117 Tonilite	5Q128 Tonilite	5Q129 Tonilite
SiO ₂	63.87	63.94	65.80	63.91	63.53	64.36	65.15	64.69	61.37	64.31	60.53
TiO ₂	0.23	0.30	0.20	0.28	0.22	0.28	0.21	0.21	0.32	0.23	0.31
Al ₂ O ₃	18.50	18.02	18.06	17.75	18.26	17.49	17.10	18.18	19.84	18.54	19.70
Fe ₂ O ₃	2.20	2.83	2.19	2.90	2.65	2.67	2.24	1.99	2.82	2.07	2.64
FeOt	2.45	3.14	2.43	3.22	2.95	2.97	2.49	2.21	3.13	2.30	2.93
MnO	0.06	0.06	0.05	0.05	0.05	0.06	0.06	0.07	0.07	0.07	0.08
MgO	1.26	1.61	1.13	1.49	1.41	1.66	1.21	1.22	1.53	1.27	1.58
CaO	4.72	4.91	5.17	5.96	3.69	5.71	4.34	4.10	6.44	5.11	6.57
Na ₂ O	5.16	4.84	4.97	4.52	6.62	4.74	5.41	5.44	4.83	5.11	5.36
K ₂ O	1.62	1.18	1.25	0.98	1.01	0.99	1.45	1.55	0.90	0.91	1.00
P ₂ O ₅	0.12	0.21	0.16	0.17	0.13	0.15	0.11	0.05	0.12	0.18	0.14
LOI	1.63	1.57	1.19	1.37	1.65	1.53	2.07	2.17	1.55	1.52	1.72
Total	99.37	99.47	100.17	99.38	99.22	99.64	99.35	99.67	99.80	99.30	99.60
Mg#	0.531	0.530	0.506	0.504	0.513	0.552	0.516	0.548	0.518	0.549	0.542
Sc	4.470	6.036	4.276	5.612	4.547	5.866	4.208	3.868	6.479	4.034	6.372
V	28.760	43.317	31.640	46.180	37.105	47.360	31.180	22.880	53.84	38.36	54.01
Cr	14.898	18.602	16.266	13.298	16.988	28.080	22.960	25.560	10.33	5.723	7.24
Co	17.896	16.912	20.080	15.084	24.413	15.032	19.912	21.720	6.373	4.976	6.216
Ni	5.018	7.048	5.182	5.076	5.915	12.780	8.320	7.216	5.956	3.87	7.7
Cu	4.024	13.470	5.780	4.720	5.303	4.818	4.930	6.540	3.274	2.862	2.943
Zn	30.40	45.52	33.82	34.00	48.79	69.84	60.38	44.44	44.97	21.6	53.52
Ga	15.906	18.258	17.774	18.970	17.585	19.224	15.808	14.176	53.66	48.39	49.58
Rb	51.500	32.846	32.060	25.000	43.289	28.380	55.220	44.780	24.83	16.96	29.77
Sr	1197	1418	1295	1459	608.31	1592	1074	986.60	1536	1403	1814
Y	3.696	5.350	5.376	5.786	3.933	5.102	3.992	3.356	7.265	4.117	5.402
Zr	71.88	79.46	68.02	70.90	68.96	88.76	72.12	64.16	101.80	61.38	71.24
Nb	3.174	3.363	4.042	3.784	3.286	3.858	3.088	2.682	5.129	4.236	3.454
Cs	1.067	1.736	2.664	3.802	1.151	1.820	2.162	0.862	1.825	1.193	1.964
Ba	1311	1026	1280	1241	330.23	1031	725.40	1283	989.7	904.4	902.3
La	8.054	12.837	10.858	16.608	14.201	13.024	11.542	9.502	24.15	11.37	15.64
Ce	14.53	24.05	19.95	30.46	26.07	23.48	20.78	17.70	42.45	20.67	27.18
Pr	1.742	2.882	2.226	3.430	2.876	2.648	2.330	1.984	4.589	2.324	3.218
Nd	6.658	10.757	8.214	12.850	10.543	9.886	8.856	7.556	16.09	8.405	12.01
Sm	1.247	1.953	1.420	2.136	1.706	1.709	1.462	1.286	2.491	1.406	2.101
Eu	0.501	0.709	0.561	0.717	0.482	0.644	0.530	0.502	0.902	0.555	0.811
Gd	0.979	1.568	1.168	1.635	1.201	1.385	1.125	0.985	2.026	1.111	1.693
Tb	0.121	0.193	0.156	0.199	0.147	0.175	0.136	0.120	0.247	0.132	0.204
Dy	0.685	1.052	0.928	1.073	0.781	0.949	0.747	0.676	1.383	0.776	1.103
Ho	0.130	0.197	0.180	0.204	0.152	0.186	0.140	0.125	0.272	0.151	0.211
Er	0.376	0.551	0.544	0.593	0.426	0.532	0.415	0.358	0.777	0.439	0.591
Tm	0.055	0.079	0.082	0.084	0.059	0.075	0.060	0.049	0.115	0.067	0.084
Yb	0.361	0.523	0.539	0.561	0.399	0.496	0.388	0.332	0.723	0.440	0.535
Lu	0.060	0.081	0.087	0.081	0.061	0.075	0.061	0.054	0.114	0.073	0.084
Hf	1.758	1.943	1.728	1.762	1.680	2.162	1.753	1.691	2.559	1.643	1.851
Ta	0.190	0.193	0.190	0.223	0.183	0.195	0.161	0.207	0.222	0.2095	0.123
Pb	11.090	13.304	13.932	8.338	4.099	12.822	9.746	98.460	14.38	7.887	11.50
Th	2.222	4.350	2.668	3.770	3.787	3.308	2.722	2.682	6.700	2.718	4.059
U	1.224	0.902	1.942	1.150	0.809	0.840	0.658	0.954	1.921	0.949	0.822

laser-ablation microprobe, attached to a Neptune multi-collector ICP-MS, at Chinese University of Geosciences, Wuhan. Instrumental conditions and data acquisition were comprehensively described by [Hu et al. \(2012\)](#).

Zircon crystals from a plutonic tonalite sample (5Q117) have clear oscillatory bands of magmatic origin in the cathodoluminescence (CL) images ([Fig. 9a](#)). Fourteen analyses by SHRIMP II give ages of 435–412 Ma with a weighted mean of 423 ± 4 Ma (MSWD = 1.2) ([Fig. 9c](#)). Zircons from garnetite (10DL12) and garnet-bearing tonalite

(10DL19 and 5Q122) exhibit complicated internal structures largely of magmatic origin, with some crystals containing metamorphic cores apparent in CL images, but the age data for the metamorphic cores and magmatic rims have no significant difference ([Fig. 9b](#)). These features are most probably due to high-pressure crystallization. Twenty-three analyses of garnetite sample (10DL12) by LA-ICP-MS yielded ages of 416–438 Ma with a mean of 427 ± 3 Ma. Twenty-four analyses of 10QL19 by LA-ICP-MS gave ages of 426–440 Ma with a mean of 431 ± 3 Ma (MSWD

Table 3

Whole-rock major and trace element abundances of mafic granulites.

Sample	DL-24	DL-39	DL-40	DL-41	DL-43	DL-56	DL-59	5Q108	5Q111	5Q114
SiO ₂	44.90	43.23	44.95	47.36	45.03	44.31	44.08	44.29	44.70	44.27
TiO ₂	0.45	0.37	0.44	0.61	0.22	0.71	0.65	0.66	0.56	0.58
Al ₂ O ₃	19.51	16.65	22.12	18.26	15.46	20.93	18.66	19.57	21.80	21.79
Fe ₂ O ₃	11.87	13.89	11.31	11.93	8.90	14.75	15.12	13.56	12.26	13.28
MnO	0.18	0.17	0.21	0.23	0.19	0.28	0.26	0.24	0.26	0.30
MgO	5.62	9.41	5.47	5.59	10.08	4.96	6.81	5.72	4.75	4.91
CaO	12.65	11.99	12.08	8.29	15.52	10.72	12.11	11.82	10.31	10.24
Na ₂ O	2.27	0.99	2.00	3.25	1.34	2.41	1.46	1.26	2.91	2.79
K ₂ O	0.27	0.53	0.32	0.46	0.78	0.3	0.21	0.54	0.44	0.48
P ₂ O ₅	0.17	0.07	0.34	0.27	0.06	0.32	0.10	0.13	0.30	0.37
LOI	0.55	2.56	0.76	2.96	1.65	0.72	0.16	1.95	1.17	1.02
Total	98.43	99.86	100.01	99.21	99.22	100.40	99.62	99.74	99.46	100.02
Mg#	0.48	0.57	0.49	0.48	0.69	0.40	0.47	0.45	0.43	0.42
Sc	37.76	56.98	28.36	40.08	69.76	43.54	52.00	49.4	36.17	36.77
V	370.6	517.4	264.7	295.2	247.8	293.6	453.2	424.5	234.3	242.7
Cr	34.02	39.54	28.02	78.70	189.8	10.99	14.20	29.33	25.19	7.30
Co	45.26	64.70	42.97	39.30	42.24	48.08	51.06	39.19	27.28	28.15
Ni	19.74	38.44	7.93	16.87	39.10	5.20	11.87	17.52	12.69	4.76
Cu	68.60	59.46	126.6	56.14	165.0	183.4	88.06	106.1	47.56	30.74
Zn	135.5	81.98	95.05	105.2	127.0	118.6	108.8	103.7	109.2	113.8
Ga	26.84	16.45	19.84	18.27	14.66	22.50	21.08	23.71	26.12	27.39
Rb	11.05	18.09	18.82	19.71	33.06	13.40	7.33	16.42	12.93	16.99
Sr	1013	355.8	834.5	599.8	514.2	806.6	605.2	882.1	884.2	861.1
Y	5.35	3.64	8.00	9.24	5.04	16.44	7.75	8.85	15.03	11.08
Zr	7.45	3.81	7.34	10.02	9.64	7.96	7.78	8.05	9.10	12.50
Nb	0.46	0.22	0.78	0.86	0.24	1.03	0.33	0.84	1.64	2.21
Cs	0.58	0.99	1.00	0.67	1.10	0.52	0.25	0.45	0.74	0.60
Ba	76.00	128.3	98.52	108.9	309.6	351.2	49.84	64.22	108.4	143.1
La	4.76	1.30	7.04	7.03	3.18	7.23	2.53	3.66	13.20	13.66
Ce	10.20	2.58	16.06	14.21	6.53	16.12	5.75	8.21	31.18	29.52
Pr	1.27	0.40	2.29	1.93	0.88	2.57	0.92	1.26	4.58	4.07
Nd	5.75	2.17	10.88	9.05	4.21	13.32	5.02	6.30	20.83	17.94
Sm	1.29	0.65	2.30	2.03	1.08	3.41	1.49	1.67	4.36	3.48
Eu	0.77	0.30	0.85	1.01	0.43	1.18	0.67	0.78	1.38	1.37
Gd	1.25	0.70	1.99	1.99	1.02	3.33	1.56	1.73	3.79	2.94
Tb	0.18	0.11	0.27	0.28	0.15	0.49	0.23	0.26	0.51	0.55
Dy	1.08	0.71	1.61	1.78	0.97	3.18	1.59	1.72	3.06	2.19
Ho	0.22	0.15	0.32	0.37	0.20	0.66	0.32	0.36	0.62	0.46
Er	0.62	0.44	0.92	1.08	0.61	1.92	0.95	1.04	1.76	1.25
Tm	0.09	0.06	0.13	0.15	0.09	0.27	0.13	0.15	0.25	0.19
Yb	0.56	0.42	0.83	0.98	0.56	1.73	0.87	0.89	1.49	1.11
Lu	0.09	0.06	0.12	0.15	0.09	0.25	0.13	0.14	0.23	0.18
Hf	0.25	0.16	0.25	0.32	0.39	0.34	0.25	0.27	0.36	0.74
Ta	0.11	0.09	0.10	0.11	0.20	0.09	0.12	0.11	0.10	0.14
Pb	2.90	2.35	2.69	4.18	8.56	3.16	6.10	2.54	2.97	3.24
Th	0.50	0.09	0.24	0.37	0.79	0.40	0.17	0.13	0.40	0.62
U	0.06	0.03	0.08	0.20	0.34	0.18	0.11	0.13	0.17	0.25

= 0.35), and twenty-one analyses of 16 zircon grains from 5Q122 by SHRIMP yield 400–417 Ma with a mean at 410 ± 4 Ma (MSWD = 0.47). These results, together with the data from Yu et al. (2012), suggest that partial melting of eclogite must have taken place over a period of ~ 25 Myrs (435–410 Ma), which overlaps the peak UHP metamorphic and exhumation ages of the belt (Song et al., 2005a,b, 2006; Mattinson et al., 2006; Zhang et al., 2010).

Zircons from 5Q117 with U–Pb age of 423 Ma yield initial $^{176}\text{Hf}/^{177}\text{Hf}$ ratios of 0.282752–0.282876, $\varepsilon_{\text{Hf}}(t)$ values 8.45–12.67 and young model ages (T_{DM1}) 535–700 Ma with a weighted mean of 637 ± 27 Ma (Table 7). The positive $\varepsilon_{\text{Hf}}(t)$ values close to those of the depleted mantle at the

time of zircon crystallization indicate that the adakitic magmas were derived from melting of a juvenile basaltic crust, most probably an oceanic crust associated with the Neoproterozoic to Early Paleozoic Qilian Ocean (e.g. Song et al., 2013).

5. DISCUSSION AND IMPLICATIONS

5.1. Rutile may not be a residual phase during eclogite partial melting

Rutile is the primary host for HFSEs in the subducting ocean crust under eclogite facies conditions. The process of

Table 4
Sr–Nd isotopic analyses for mafic granulite, tonalite/trondhjemite melt, and tonalite pluton in the SDB, the N. Qaidam UHPM belt.

Sample	Rock type	Rb (ppm)	Sr (ppm)	$^{87}\text{Rb}/^{86}\text{Sr}$	$^{87}\text{Sr}/^{86}\text{Sr}$	2σ	I_{Sr} (420)	Sm (ppm)	Nd (ppm)	$^{147}\text{Sm}/^{144}\text{Nd}$	$^{143}\text{Nd}/^{144}\text{Nd}$	2σ	Nd (0)	$f_{\text{Sm/Nd}}$	ε_{Nd} (420)	T_{DM} (Ga)
5Q108	Mafic granulite	16.42	882	0.05398	0.706235	25	0.70591	1.674	6.297	0.1607	0.512597	13	-0.802	-0.08	1.13	1.59
5Q111	Mafic granulite	12.93	884	0.04241	0.704687	17	0.70443	4.356	20.83	0.1264	0.512543	8	-1.854	-0.19	1.91	1.06
5Q114	Mafic granulite	16.99	861	0.05722	0.705910	24	0.70557	3.481	17.94	0.1173	0.512551	8	-1.701	-0.17	2.55	0.95
07DL39	Mafic granulite	18.09	356	0.14745	0.705837	10	0.70496	0.65	2.17	0.1817	0.512746	11	2.107	0.21	2.91	1.92
07DL43	Mafic granulite	33.06	514	0.18645	0.708258	11	0.70714	1.08	4.20	0.1554	0.512531	10	-2.087	-0.21	0.13	1.62
07DL56	Mafic granulite	13.40	807	0.04818	0.705072	10	0.70478	3.42	13.32	0.1552	0.512617	11	-0.410	-0.04	1.81	1.39
5Q115	Tonalite melt	3.19	751	0.01232	0.704136	20	0.70406	1.301	7.646	0.1029	0.512484	12	-3.010	-0.30	2.02	0.92
5Q116	Tonalite melt	25.92	758	0.09913	0.706172	13	0.70558	1.817	10.9	0.1008	0.512483	10	-3.016	-0.30	2.13	0.90
5Q123	Tonalite melt	96.52	746	0.37506	0.709716	12	0.70747	1.117	6.146	0.1099	0.512506	11	-2.581	-0.26	2.07	0.95
5Q126	Tonalite melt	38.75	921	0.12208	0.704658	17	0.70393	2.268	15.07	0.0910	0.512508	6	-2.535	-0.25	3.13	0.80
5Q128	Tonalite melt	16.96	1403	0.03506	0.704339	15	0.70413	1.406	8.405	0.1011	0.512491	7	-2.859	-0.29	2.26	0.89
5Q129	Tonalite melt	29.77	1814	0.04759	0.704715	21	0.70443	2.101	12.01	0.1057	0.512522	7	-2.266	-0.23	2.61	0.89
07DL30	Tonalite melt	32.85	1418	0.06720	0.706095	10	0.70569	1.96	10.75	0.1102	0.512492	12	-2.848	-0.28	1.79	0.97
5Q117	Tonalite pluton	24.83	1536	0.04688	0.704644	17	0.70436	2.491	16.09	0.0936	0.512501	7	-2.665	-0.27	2.86	0.82
07DL42	Tonalite pluton	25.00	1459	0.04971	0.704124	13	0.70383	2.14	12.86	0.1006	0.512513	13	-2.438	-0.24	2.71	0.86
07DL47	Tonalite pluton	43.29	608	0.20637	0.706731	12	0.70550	1.706	10.543	0.0978	0.512478	11	-3.121	-0.31	2.18	0.88
07DL48	Tonalite pluton	28.38	1592	0.05171	0.704588	12	0.70428	1.709	9.886	0.1045	0.512540	12	-1.912	-0.19	3.03	0.85
07DL51	Tonalite pluton	55.22	1074	0.14910	0.706394	10	0.70550	1.46	8.86	0.0996	0.512501	12	-2.672	-0.27	2.53	0.87

$\varepsilon_{\text{Nd}} = ((^{143}\text{Nd}/^{144}\text{Nd})_s/(^{143}\text{Nd}/^{144}\text{Nd})_{\text{CHUR}} - 1) \times 10000$, $f_{\text{Sm/Nd}} = (^{147}\text{Sm}/^{144}\text{Nd})_s/(^{147}\text{Sm}/^{144}\text{Nd})_{\text{CHUR}} - 1$, where s = sample, $(^{143}\text{Nd}/^{144}\text{Nd})_{\text{CHUR}} = 0.512638$, $(^{147}\text{Sm}/^{144}\text{Nd})_{\text{CHUR}} = 0.1967$.

The model ages (TDM) were calculated using a linear isotopic ratio growth equation: $T_{\text{DM}} = 1/\lambda \ln(((^{143}\text{Nd}/^{144}\text{Nd})_s - 0.51315)/(^{147}\text{Sm}/^{144}\text{Nd})_s - 0.2137))$.

5.2. The primary adakite melt may not be depleted in HFSEs

The above analysis implies that the primary adakite melts should not be depleted in Ti and other HFSEs (unless their sources were depleted in these elements), which seems at odds with the common perception, but may actually be consistent with melt evolution processes. At high pressures, the first or primary liquidus phase is likely to be garnet as manifested by the garnetite cumulate (Fig. 2i). Because Ti and other HFSEs are significantly more compatible or less incompatible than otherwise similarly incompatible elements in garnet (Klemme et al., 2002), it is thus straightforward that the garnetite, i.e., the garnet cumulate from the evolving adakite melt, should inherit trace element

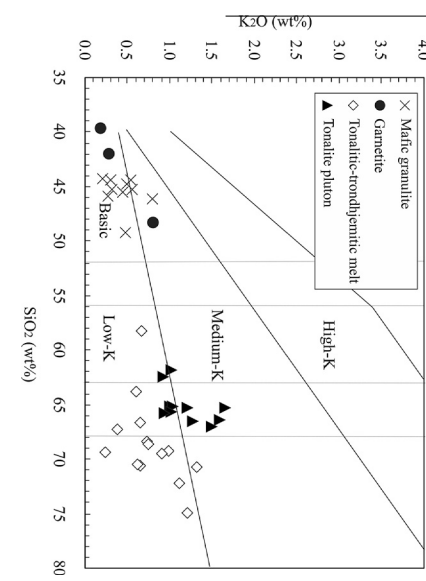


Fig. 4. Plot of K_2O versus SiO_2 for mafic granulite, garnetite, tonalite and trondhjemite melts.

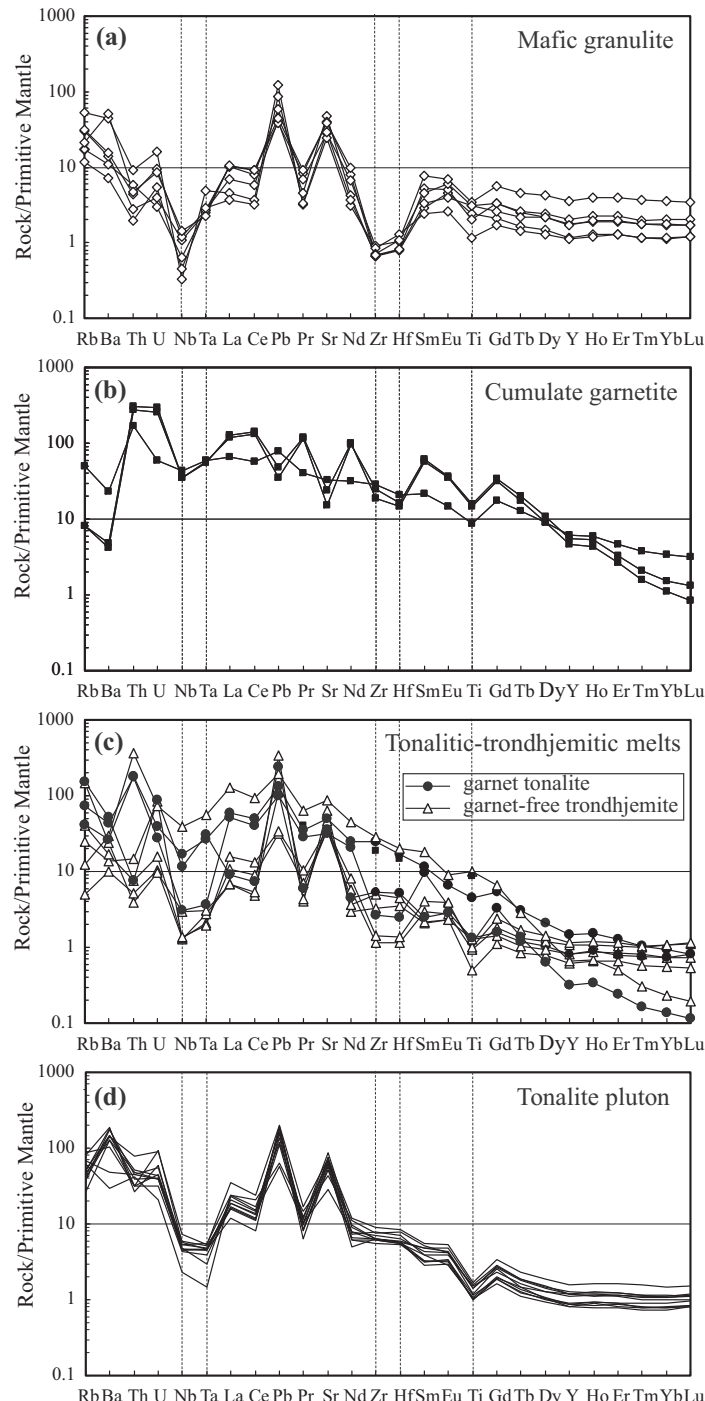


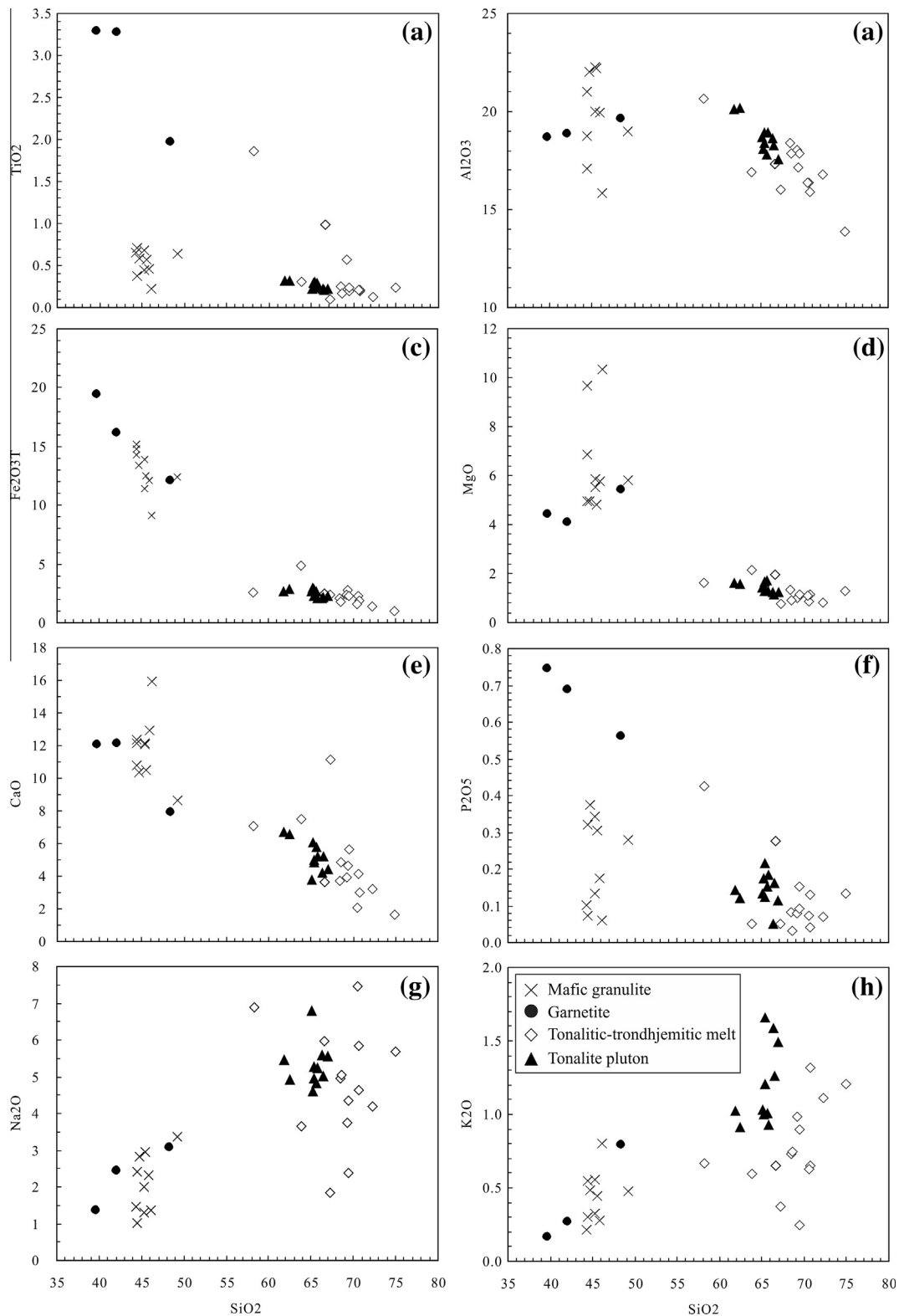
Fig. 5. Primitive mantle normalized (Sun and McDonough, 1989) trace element diagrams for (a): mafic HP granulite (b): cumulate garnetite (c): tonalitic-trondhjemite melts, and (d): tonalite pluton.

signatures of primary adakite melts with depleted HREEs without significant depletion in HFSEs (Fig. 5b).

5.3. Adakite signatures result from garnetite fractionation

It follows from the above discussion that the adakite geochemical signatures (Fig. 5d; depletion in HREEs and HFSEs and enrichment in LILEs) result from several

genetically related processes: (1) The depletion in HREEs is inherited from the parental adakite melt whose HREE-depletion results from garnet as a residual phase during melting. (2) The relative depletion of HFSEs results from garnet crystallization as evidenced by the garnetite cumulate (Fig. 2i and Fig. 5b), which, in the absent of rutile, is the major Ti host at high pressures as evidenced by the abundant rutile exsolution in UHPM garnet crystals (see

Fig. 6. Major element oxide variations of all rock-types plotted against SiO₂ content.

Song et al., 2005a). The rutile lamellae in garnet (Fig. 2j) may also be of exsolution origin, but the size and distribution patterns of the rutile lamellae in these garnet crystals may differ from those of metamorphic origin. This is an

important hypothesis to be further studied and tested. We cannot yet rule out the magmatic origin of the rutile (Fig. 2j-l) if TiO₂ content in melts are in excess of 3–4 wt% for the felsic liquids (see Ryerson and Watson,

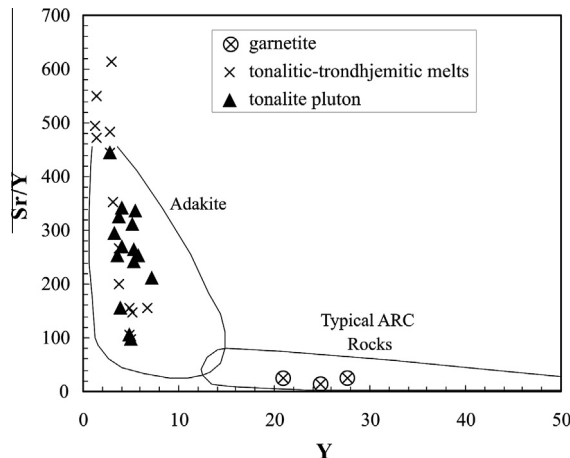


Fig. 7. Y versus Sr/Y diagram for various lithologies of garnetite, tonalite and trondhjemite melts and tonalite pluton in the Dulan UHPM terrane.

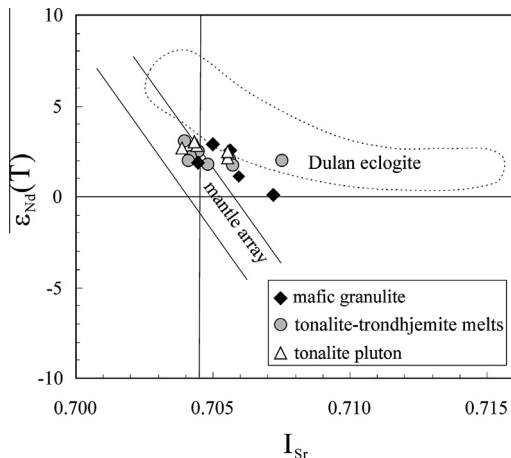


Fig. 8. $\epsilon_{\text{Nd}}(T)$ vs. I_{Sr} plot for the mafic HP granulite, tonalitic-trondhjemite melts and the tonalite pluton from the Dulan terrane. The NDB eclogite data field are from an ophiolite sequence (cumulate + basaltic) (Zhang et al., 2008).

1987) (also see below). (3) The relative enrichments of LILEs and LREEs probably result from breakdowns of hydrous phases stable under eclogite conditions (e.g., white mica and epidote group minerals) (see Xiao et al., 2012, 2013) during eclogite decompression melting at granulite facies conditions during exhumation (see below).

5.4. Tonalite-trondhjemite (adakitic) magma generation by decompression and dehydration melting of eclogite

Adakite genesis in modern arc settings has usually been linked to unusual conditions (e.g., high shear stresses, very young (<25 Ma) oceanic lithosphere, subduction initiation, slab tearing leading to the opening of an asthenospheric window, or shallowing of subduction angle) of the subducting oceanic plate (Kay, 1978; Sajona et al., 1993; Peacock et al., 1994; Gutscher et al., 2000; Yogodzinski et al.,

2001). The tonalite-trondhjemite (adakitic) magma in this study must have an unusual mechanism/environment in association with continental subduction and exhumation: (1) The volume of the adakitic magmas requires melting of volumetrically significant ocean crust metamorphosed to eclogite. (2) The protolith of the eclogites is likely dominated by low-K tholeiitic and/or gabbroic rocks because all the melts are of low-K and high-Na composition, which rules out eclogites of the 850–820 Ma CFB protolith (Song et al., 2010). (3) Their melting must be accomplished through decompression with the assistances of dehydration and heating.

We hypothesize that the UHP metamorphosed basaltic and gabbroic rocks in the ophiolite sequences in the Dulan terrane (Zhang et al., 2008, 2009; Song et al., 2003a,b, 2009) are the protolith of the adakitic melts, with the melting taking place during exhumation along the continental subduction channel (also see below). The depleted whole-rock Nd isotopes, as well as Hf isotope ($\epsilon_{\text{Hf}} 8.45–12.67$) and young model ages (T_{DM1}) 535–700 Ma of zircons, suggest these adakitic melts are consistent with the ocean crust protolith as elaborated above.

In continental subduction zones, thermal relaxation of thickened crust and its decompression are the major mechanisms for generating felsic magmas (e.g., Vanderhaeghe and Teyssier, 2001; Wallis et al., 2005; Labrousse et al., 2011). Hermann et al. (2001) suggested that partial melting could start at the very initiation of the exhumation of continental crust at ultrahigh pressures. In our samples, the rock textures indicate that partial melting of the eclogite took place during exhumation as reflected by decompression of garnet and omphacite during the transition from eclogitic to granulitic facies conditions (Fig. 2 a,c,d,e). As argued above, the positive zircon Hf isotope ($\epsilon_{\text{Hf}}(t) = 9–12$) and young T_{DM1} age (637 Ma) suggest that these magmas were most probably derived from melting of an oceanic crust (vs. continental crustal rocks). Zircon SHRIMP dating reveals that partial melting of eclogite occurred simultaneously within the period of continental subduction and exhumation (~435–410 Ma). We thus infer that the eclogite melting is both a decompression (from ca. 3.3 GPa to 1.9–2.0 GPa) and heating (from 630–730 °C to 870–950 °C) process from UHP eclogite to HP granulite (Fig. 10). Generally, the >200 °C temperature increase during exhumation is probable and with the assistance of fluids released from decomposition of lawsonite, zoisite and phengite (see below), it becomes straightforward that the eclogite melts during exhumation/decompression. This is apparently characteristic of all UHPM terrains (continental collision/subduction) on Earth (e.g. Hacker and Peacock, 1995; Chopin, 2003). The heat is expected to come from the hot mantle, may indeed associated with slab break off. Because of eclogite decompression melting during exhumation, it is expected that such adakite melts have low Cr, Ni and Mg# (mostly < 0.6) without interaction with mantle peridotites.

Continental subduction following seafloor subduction is a natural consequence of ocean basins with a passive continental margin and has been demonstrated to be the case for the prior history of the North Qaidam UHPM belt (Song et al., 2006; Zhang et al., 2008). The former ocean

Table 5

U–Th–Pb SHRIMP analyses for zircons from tonalite pluton (Q5-117) and garnet-tonalite (Q5-122).

Spot	U ppm	Th ppm	$^{232}\text{Th}/^{238}\text{U}$	$^{206}\text{Pb}_c$ (%)	$^{206}\text{Pb}^*$ (ppm)	$^{207}\text{Pb}^*/^{206}\text{Pb}^*$	$\pm\%$	$^{207}\text{Pb}^*/^{235}\text{U}$	$\pm\%$	$^{206}\text{Pb}^*/^{238}\text{U}$	$\pm\%$	$^{206}\text{Pb}/^{238}\text{Uage}$ (Ma)
Q5-117-1.1	357	119	0.34	0.75	21.8	0.0555	4.6	0.54	4.9	0.0671	1.6	419 ± 7
Q5-117-2.1	823	201	0.25	0.19	46.7	0.0558	1.5	0.51	2.2	0.0659	1.5	412 ± 6
Q5-117-3.1	298	102	0.36	1.01	17.3	0.0512	7.0	0.47	7.2	0.0671	1.7	418 ± 7
Q5-117-4.1	51	19	0.39	4.74	3.0	0.0371	7.4	0.34	7.5	0.0660	2.9	412 ± 12
Q5-117-5.1	482	132	0.28	0.43	29.0	0.0553	2.8	0.53	3.3	0.0698	1.6	435 ± 7
Q5-117-6.1	1136	301	0.27	0.21	67.6	0.0548	1.4	0.52	2.1	0.0691	1.5	431 ± 6
Q5-117-7.1	892	158	0.18	0.41	52.7	0.0544	2.4	0.51	2.8	0.0685	1.5	427 ± 6
Q5-117-8.1	610	165	0.28	0.31	35.7	0.0559	2.0	0.52	2.5	0.0680	1.6	424 ± 6
Q5-117-9.1	722	230	0.33	0.32	42.0	0.0543	2.3	0.50	2.7	0.0674	1.6	421 ± 6
Q5-117-10.1	429	111	0.27	0.61	25.9	0.0554	4.2	0.53	4.5	0.0697	1.6	434 ± 7
Q5-117-11.1	661	174	0.27	0.74	39.0	0.0554	5.0	0.52	5.3	0.0681	1.6	425 ± 7
Q5-117-12.1	411	99	0.25	1.09	25.0	0.0571	5.7	0.55	6.0	0.0698	1.9	415 ± 8
Q5-117-13.1	279	75	0.28	1.50	17.1	0.0642	5.7	0.62	5.9	0.0687	1.8	429 ± 7
Q5-117-14.1	428	83	0.20	0.74	24.1	0.0532	4.4	0.48	4.7	0.0669	1.6	415 ± 8
Q5-122-1.1	59	0.9	0.016	6.43	3.57	0.054	30	0.48	30	0.0653	3	408 ± 12
Q5-122-1.2	88	0.4	0.004	3.41	5.26	0.07	16	0.64	16	0.067	2.6	418 ± 11
Q5-122-2.1	220	2.3	0.011	0.93	12.6	0.0611	6.6	0.559	6.9	0.0663	1.9	414 ± 8
Q5-122-2.2	113	0.2	0.002	3.37	6.54	0.0581	16	0.52	16	0.0649	2.4	406 ± 9
Q5-122-3.1	23	0.1	0.003	4.13	1.37	0.133	22	1.21	22	0.0661	4.2	413 ± 17
Q5-122-4.1	195	2.9	0.016	2.51	11.1	0.0538	12	0.479	13	0.0646	2	404 ± 8
Q5-122-5.1	150	1.6	0.011	3.49	9.07	0.0519	18	0.484	18	0.0677	2.3	423 ± 9
Q5-122-6.1	146	0.3	0.002	1.81	8.38	0.0605	12	0.547	12	0.0656	2.2	409 ± 9
Q5-122-7.1	193	2.1	0.011	1.91	10.8	0.0544	9.7	0.48	9.9	0.064	2	400 ± 8
Q5-122-8.1	729	182.7	0.259	0.76	40.9	0.0584	5	0.522	5.2	0.0649	1.6	405 ± 6
Q5-122-9.1	126	1.2	0.010	3.77	7.24	0.055	18	0.484	18	0.0641	2.5	401 ± 10
Q5-122-10.1	90	0.5	0.005	2.91	5.28	0.068	17	0.62	17	0.0663	3.9	414 ± 16
Q5-122-11.1	170	0.3	0.002	2.00	9.76	0.0648	8.9	0.585	9.2	0.0656	2.2	410 ± 9
Q5-122-12.1	143	0.5	0.003	0.61	8.21	0.0749	6.8	0.688	7.1	0.0666	2.1	416 ± 9
Q5-122-13.1	131	0.3	0.002	2.14	7.61	0.0661	7.7	0.604	8	0.0663	2.1	414 ± 9
Q5-122-14.1	450	285.1	0.655	0.71	25.9	0.0596	5	0.548	5.3	0.0666	1.7	416 ± 7
Q5-122-15.1	108	0.5	0.004	6.64	6.46	0.046	35	0.41	36	0.0649	2.9	406 ± 11
Q5-122-16.1	88	0.4	0.004	3.96	5.07	0.063	18	0.56	18	0.0643	4.3	402 ± 17
Q5-122-17.1	128	0.3	0.002	1.27	7.39	0.0635	7.9	0.58	8.2	0.0662	2.2	413 ± 9
Q5-122-18.1	103	0.7	0.007	0.94	5.77	0.0806	7.3	0.722	7.7	0.0649	2.3	406 ± 9

Radiogenic lead Pb* corrected for common Pb using ^{204}Pb . All errors are 1σ of standard deviation.

Table 6

U-Th-Pb analyses by LA-ICPMS for zircons from garnetite (DL12) and garnet-tonalite (DL19).

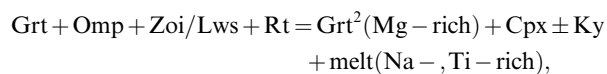
Analysis	Th (ppm)	U (ppm)	Pb	Th/U	$^{207}\text{Pb}/^{206}\text{Pb}$	$^{207}\text{Pb}/^{235}\text{U}$	$^{206}\text{Pb}/^{238}\text{U}$	$^{207}\text{Pb}/^{206}\text{Pb}$ Age (Ma)	$^{207}\text{Pb}/^{235}\text{U}$ Age (Ma)	$^{206}\text{Pb}/^{238}\text{U}$ Age (Ma)
DL12-01	87.84	870.31	58.88	0.10	0.05512 ± 0.00149	0.52339 ± 0.01471	0.06886 ± 0.00107	417 ± 36	427 ± 10	429 ± 6
DL12-02	15.01	129.07	8.63	0.12	0.05527 ± 0.00266	0.51620 ± 0.02482	0.06773 ± 0.00119	423 ± 76	423 ± 17	422 ± 7
DL12-03	14.25	114.46	7.85	0.12	0.05541 ± 0.00379	0.52865 ± 0.03612	0.06918 ± 0.00123	429 ± 121	431 ± 24	431 ± 7
DL12-04	24.66	346.07	22.58	0.07	0.05509 ± 0.00176	0.50872 ± 0.01661	0.06696 ± 0.00107	416 ± 45	418 ± 11	418 ± 6
DL12-05	47.11	524.83	35.70	0.09	0.05520 ± 0.00155	0.52772 ± 0.01537	0.06932 ± 0.00108	420 ± 38	430 ± 10	432 ± 7
DL12-06	15.24	104.37	7.31	0.15	0.05574 ± 0.00278	0.5409 ± 0.02691	0.07036 ± 0.00126	442 ± 79	439 ± 18	438 ± 8
DL12-07	31.24	311.74	21.34	0.10	0.05564 ± 0.00188	0.53377 ± 0.01837	0.06957 ± 0.00113	438 ± 48	434 ± 12	434 ± 7
DL12-08	7.29	132.78	8.72	0.05	0.05518 ± 0.00335	0.51374 ± 0.03113	0.06752 ± 0.00119	420 ± 104	421 ± 21	421 ± 7
DL12-09	12.71	97.10	6.74	0.13	0.05558 ± 0.00322	0.53482 ± 0.03086	0.06977 ± 0.00128	436 ± 96	435 ± 20	435 ± 8
DL12-10	5.57	129.01	8.56	0.04	0.05530 ± 0.00297	0.52162 ± 0.02796	0.0684 ± 0.00121	424 ± 88	426 ± 19	427 ± 7
DL12-11	15.99	185.53	12.22	0.09	0.05513 ± 0.00230	0.50936 ± 0.02135	0.067 ± 0.00113	417 ± 63	418 ± 14	418 ± 7
DL12-12	77.03	321.85	23.06	0.24	0.05565 ± 0.00187	0.53826 ± 0.01844	0.07013 ± 0.00113	438 ± 48	437 ± 12	437 ± 7
DL12-13	55.48	167.27	11.86	0.33	0.05550 ± 0.00340	0.51668 ± 0.03166	0.0675 ± 0.00117	432 ± 106	423 ± 21	421 ± 7
DL12-14	10.37	175.70	11.49	0.06	0.05511 ± 0.00239	0.51036 ± 0.02213	0.06715 ± 0.00115	417 ± 66	419 ± 15	419 ± 7
DL12-15	12.60	118.80	8.20	0.11	0.05550 ± 0.00263	0.53462 ± 0.02529	0.06985 ± 0.00124	432 ± 74	435 ± 17	435 ± 7
DL12-16	35.49	160.32	10.96	0.22	0.05819 ± 0.00305	0.53578 ± 0.02815	0.06677 ± 0.00114	537 ± 85	436 ± 19	417 ± 7
DL12-17	23.41	146.14	9.83	0.16	0.05521 ± 0.00261	0.51147 ± 0.0242	0.06718 ± 0.00117	421 ± 74	419 ± 16	419 ± 7
DL12-18	9.92	80.92	5.61	0.12	0.05552 ± 0.00326	0.53193 ± 0.03099	0.06948 ± 0.00131	433 ± 96	433 ± 21	433 ± 8
DL12-19	17.94	172.37	11.58	0.10	0.05528 ± 0.00281	0.51847 ± 0.02643	0.06801 ± 0.00116	424 ± 83	424 ± 18	424 ± 7
DL12-20	14.09	96.34	6.76	0.15	0.05554 ± 0.00300	0.53346 ± 0.02866	0.06965 ± 0.00129	434 ± 87	434 ± 19	434 ± 8
DL12-21	9.11	94.39	6.38	0.10	0.05537 ± 0.00314	0.52205 ± 0.02938	0.06837 ± 0.00127	427 ± 92	427 ± 20	426 ± 8
DL12-22	13.32	144.80	9.74	0.09	0.04926 ± 0.00316	0.46583 ± 0.02983	0.06857 ± 0.0012	160 ± 112	388 ± 21	428 ± 7
DL12-23	14.47	98.29	6.53	0.15	0.05505 ± 0.00315	0.5056 ± 0.02868	0.06659 ± 0.00126	414 ± 93	415 ± 19	416 ± 8
DL19-01	44.41	263.31	17.60	0.17	0.05508 ± 0.00177	0.50837 ± 0.01675	0.06692 ± 0.00108	415 ± 45	417 ± 11	418 ± 7
DL19-02	25.87	141.77	9.91	0.18	0.05572 ± 0.00345	0.53773 ± 0.03338	0.06998 ± 0.00118	441 ± 108	437 ± 22	436 ± 7
DL19-03	55.98	237.61	16.98	0.24	0.05574 ± 0.00205	0.54113 ± 0.02025	0.07039 ± 0.00114	442 ± 54	439 ± 13	439 ± 7
DL19-04	27.23	156.52	10.79	0.17	0.05541 ± 0.0023	0.52612 ± 0.02207	0.06885 ± 0.00116	429 ± 63	429 ± 15	429 ± 7
DL19-05	41.76	277.05	18.90	0.15	0.05549 ± 0.0022	0.52719 ± 0.02133	0.0689 ± 0.00109	432 ± 62	430 ± 14	430 ± 7
DL19-06	29.02	235.36	16.07	0.12	0.05547 ± 0.00191	0.52999 ± 0.01864	0.06928 ± 0.00112	431 ± 50	432 ± 12	432 ± 7
DL19-07	31.26	221.00	15.46	0.14	0.05574 ± 0.00225	0.54577 ± 0.02237	0.071 ± 0.00116	442 ± 62	442 ± 15	440 ± 7
DL19-08	32.08	148.90	10.57	0.22	0.05566 ± 0.00242	0.54022 ± 0.02364	0.07038 ± 0.00118	439 ± 67	439 ± 16	438 ± 7
DL19-09	33.44	158.05	11.15	0.21	0.05559 ± 0.0022	0.53361 ± 0.0213	0.06961 ± 0.00117	436 ± 59	434 ± 14	434 ± 7
DL19-10	31.23	147.79	10.35	0.21	0.05544 ± 0.00289	0.53175 ± 0.02781	0.06955 ± 0.00118	430 ± 86	433 ± 18	433 ± 7
DL19-11	23.92	179.92	12.17	0.13	0.05527 ± 0.00198	0.52181 ± 0.01896	0.06846 ± 0.00113	423 ± 52	426 ± 13	427 ± 7
DL19-12	25.89	168.79	11.94	0.15	0.05579 ± 0.00227	0.54745 ± 0.02243	0.07116 ± 0.0012	444 ± 61	443 ± 15	443 ± 7
DL19-13	26.72	208.22	14.17	0.13	0.05544 ± 0.00209	0.52666 ± 0.02015	0.06889 ± 0.00115	430 ± 56	430 ± 13	429 ± 7
DL19-14	39.25	262.09	17.98	0.15	0.05553 ± 0.00186	0.5294 ± 0.0181	0.06914 ± 0.00112	434 ± 48	431 ± 12	431 ± 7
DL19-15	20.44	166.79	11.36	0.12	0.05543 ± 0.00227	0.52618 ± 0.02168	0.06883 ± 0.00117	430 ± 61	429 ± 14	429 ± 7
DL19-16	40.29	284.76	19.47	0.14	0.05552 ± 0.00217	0.52809 ± 0.02091	0.06897 ± 0.00112	433 ± 59	431 ± 14	430 ± 7
DL19-17	33.13	153.00	10.59	0.22	0.05529 ± 0.00263	0.52141 ± 0.02489	0.06838 ± 0.00119	424 ± 75	426 ± 17	426 ± 7
DL19-18	24.90	141.50	9.69	0.18	0.05539 ± 0.0029	0.52242 ± 0.02737	0.0684 ± 0.0012	428 ± 85	427 ± 18	427 ± 7
DL19-19	18.20	141.04	9.54	0.13	0.05538 ± 0.00248	0.52186 ± 0.02338	0.06833 ± 0.00119	428 ± 69	426 ± 16	426 ± 7

(continued on next page)

Analysis	Th (ppm)	U (ppm)	Pb	Th/U	$^{207}\text{Pb}/^{206}\text{Pb}$	$^{207}\text{Pb}/^{235}\text{U}$	$^{206}\text{Pb}/^{238}\text{U}$	$^{207}\text{Pb}/^{206}\text{Pb}$ Age (Ma)	$^{207}\text{Pb}/^{235}\text{U}$ Age (Ma)	$^{206}\text{Pb}/^{238}\text{U}$ Age (Ma)
DL19-20	32.24	165.01	11.36	0.20	0.05552 ± 0.00209	0.52492 ± 0.01991	0.06856 ± 0.00116	433 ± 54	428 ± 13	427 ± 7
DL19-21	29.31	147.70	10.28	0.20	0.05554 ± 0.00259	0.52985 ± 0.0248	0.06917 ± 0.00119	434 ± 73	432 ± 16	431 ± 7
DL19-22	25.60	176.24	12.12	0.15	0.05543 ± 0.00255	0.5292 ± 0.0245	0.06923 ± 0.00117	430 ± 73	431 ± 16	432 ± 7
DL19-23	30.04	152.00	10.63	0.20	0.05551 ± 0.00236	0.53074 ± 0.02269	0.06933 ± 0.00118	433 ± 65	432 ± 15	432 ± 7
DL19-24	28.94	138.12	9.57	0.21	0.05557 ± 0.00253	0.52663 ± 0.02405	0.06872 ± 0.00119	435 ± 71	430 ± 16	428 ± 7

All errors are 1σ of standard deviation.

lithosphere subduction is generally cold with a geothermal gradient of $\sim 6\text{--}7\text{ }^{\circ}\text{C/km}$ (Song et al., 2007), which makes some water-bearing minerals, such as lawsonite, zoisite/epidote and phengite, remain stable at high pressure (e.g., Poli and Schmidt, 2002; Wei and Clarke, 2011; Xiao et al., 2012, 2013). Lawsonite occurs as inclusions in garnet in the North Qilian low-T eclogite (Zhang et al., 2007; Song et al., 2007), while zoisite/epidote and phengite are common phases in the Dulan eclogites (Song et al., 2003b; Zhang et al., 2008). Meanwhile, some nominally anhydrous mineral at UHP conditions can also contain certain amounts of hydroxyl (up to 3000 ppm in cpx and 1000 ppm in garnet) (e.g., Katayama and Nakashima, 2003; Song et al., 2005a). Dehydration of these minerals would provide additional amount of water (e.g., Skjerlie and Patiño Douce, 2002) to facilitate the eclogite decompression melting, probably in the form of the melting reaction:



where $\text{Grt}^2 + \text{Cpx} \pm \text{Ky}$ are residual phases as in the mafic granulite and the Grt^2 is more rich in pyrope than the eclogite garnet (Fig. 3). Igneous garnet, rutile and apatite (if the melt is highly enriched in Ti and P; see above) precipitate with sodic plagioclase in magma chamber at deep level ($>40\text{ km}$) and form the cumulate assemblage of garnetite, garnet-bearing tonalite, whilst most of the melt intrudes as plutons upward into the upper crust. Igneous garnet in the cumulates is characterized by high CaO, low MgO and low HREE, different from the garnet in eclogite and residual mafic granulite (Fig. 3).

The details of subduction and exhumation of continental crust remain unclear. Numerical modeling indicates that initiation of continental subduction will disturb the thermal structure of the subduction zone and part of the subducting oceanic slab will roll back and be accreted to the subduction channel (e.g., Beaumont et al., 2009; Li et al., 2011; Gerya, 2011), which then cause eclogitized slab start to rise driven by the bulk-buoyancy dominated by the crustal materials (i.e., granitic gneisses). The rising eclogite will rise and decompression melting will take place. On the other hand, the geochronology suggests that partial melting may have occurred in the period from approximately syn-continental subduction to $\sim 10\text{ Myrs}$ after slab breakoff (the youngest UHPM ages of the continental crust). Subsequently, the buoyant continental crust will initiate exhumation along the subduction channel carrying with it the volumetrically lesser eclogite of ocean crust protolith (Fig. 10). These eclogite blocks will undergo decompression melting and produce adakite melts with all the characteristics discussed above (see Figs. 2–5). Partial melting will also weaken the subducting slab and further promote the exhumation of the buoyant continental crust with its carried bodies of eclogite (e.g., Labrousse et al., 2011).

5.5. Implications for continental crustal growth

Generally, modern adakites are mainly located in island arcs or active continental margins that are closely associated with the seafloor subduction (e.g. Defant and

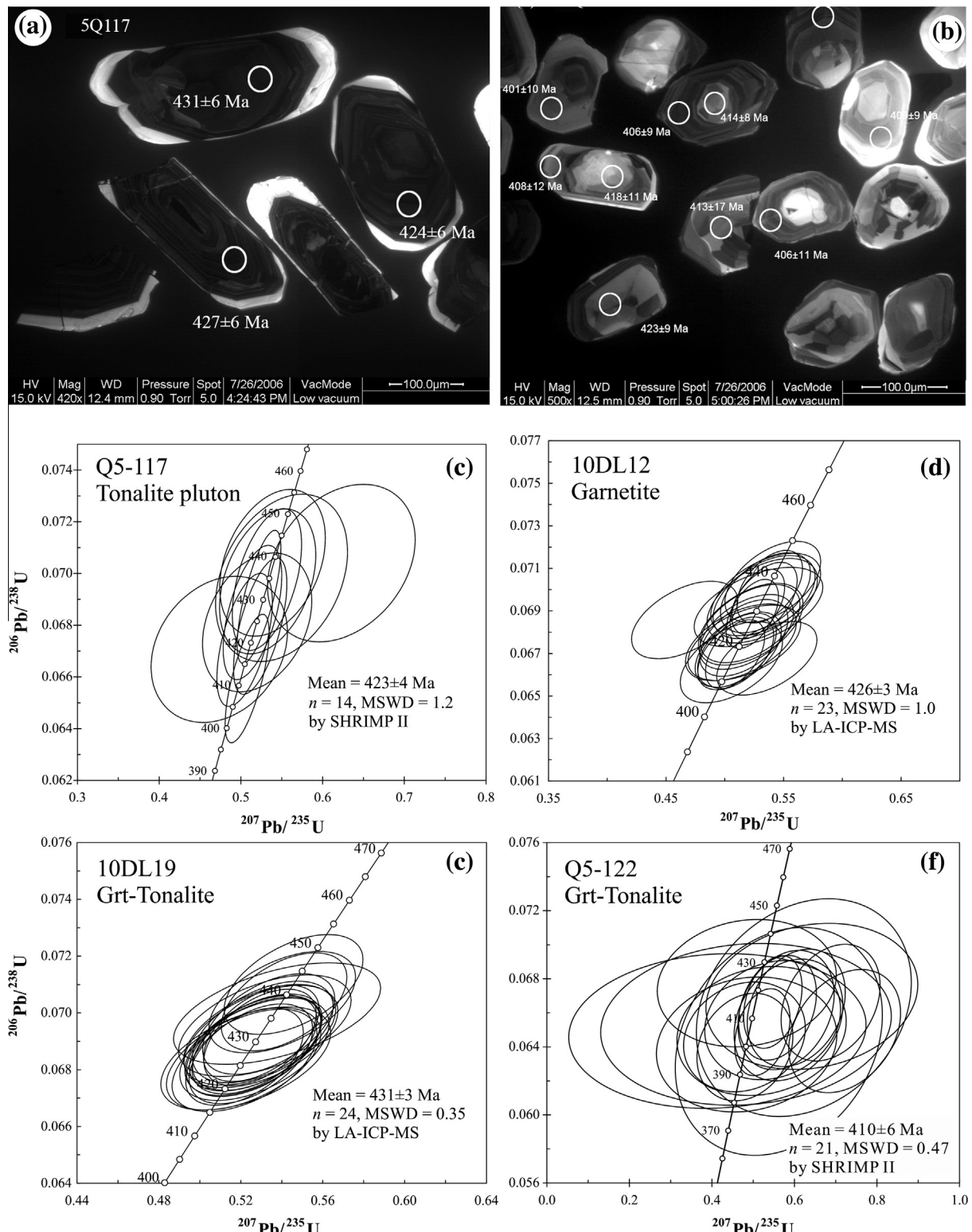


Fig. 9. Cathodoluminescent (CL) images of zircons from (a) tonalite pluton (5Q117) and (b) garnet-bearing tonalite melt (5Q122). U-Pb diagrams for zircons from: (c) tonalite pluton (sample Q5-117), (d) garnetite (10DL12), (e) and (f) garnet-bearing tonalite (sample 10DL19 and Q5-122). All plotted data are corrected using ^{204}Pb and the weighted $^{206}\text{Pb}/^{238}\text{U}$ mean ages are at the 95% confidence level.

Drummond, 1990; Castillo et al., 1999; Castillo, 2012). On the other hand, adakitic magmas have also been recognized in other orogenic belts, e.g., ~43 Ma adakitic rock in

Himalaya orogen (Zeng et al., 2011), which is several Myrs later than the UHP metamorphic ages (46–50 Ma), the 56–50 Ma adakitic rocks in the Agvanis, NE Turkey (Topuz

Table 7
Zircon Lu-Hf isotopic data for the tonalite pluton (Q5-117).

Sample	$^{176}\text{Lu}/^{177}\text{Hf}$	1σ	$^{176}\text{Lu}/^{177}\text{Hf}$	1σ	$^{176}\text{Yb}/^{177}\text{Hf}$	1σ	$\varepsilon_{\text{Hf}(t)}$ (423 Ma)	1σ	T_{DM} (Ma)	1σ	$T_{\text{DM}}/(\text{Ma})$	$f_{\text{Lu/Hf}}$
Q5-117-1	0.282780	0.000012	0.000583	0.000008	0.019333	0.000294	0.30	0.67	9.45	0.70	661	17
Q5-117-2	0.282778	0.000013	0.001221	0.000014	0.044349	0.000444	0.20	0.69	9.18	0.72	676	19
Q5-117-3	0.282801	0.000011	0.000012	0.000000	0.000397	0.000007	1.01	0.63	10.33	0.66	623	15
Q5-117-4	0.282752	0.000010	0.000582	0.000025	0.018538	0.000776	-0.71	0.62	8.45	0.65	701	13
Q5-117-5	0.282786	0.000011	0.000708	0.000007	0.024647	0.00296	0.51	0.64	9.63	0.67	655	15
Q5-117-6	0.282794	0.000010	0.000245	0.000002	0.008421	0.00055	0.79	0.61	10.04	0.64	636	13
Q5-117-7	0.282783	0.000020	0.000578	0.000043	0.016695	0.00946	0.38	0.88	9.53	0.90	658	27
Q5-117-8	0.282805	0.000012	0.000506	0.000007	0.016793	0.00202	1.18	0.67	10.35	0.69	625	17
Q5-117-9	0.282835	0.000012	0.001475	0.000051	0.052238	0.002403	2.22	0.67	11.13	0.71	599	17
Q5-117-10	0.282840	0.000016	0.001877	0.000017	0.069110	0.00862	2.41	0.75	11.21	0.78	598	22
Q5-117-11	0.282804	0.000011	0.000644	0.000009	0.021358	0.00365	1.15	0.63	10.29	0.66	628	15
Q5-117-12	0.282876	0.000015	0.001133	0.000015	0.039861	0.00518	3.67	0.73	12.67	0.76	535	21
Q5-117-12	0.282789	0.000012	0.000561	0.000014	0.018740	0.00491	0.60	0.66	9.76	0.68	649	16
Q5-117-14	0.282806	0.000010	0.000050	0.000001	0.001309	0.00037	1.20	0.62	10.50	0.65	617	14
												-1.00

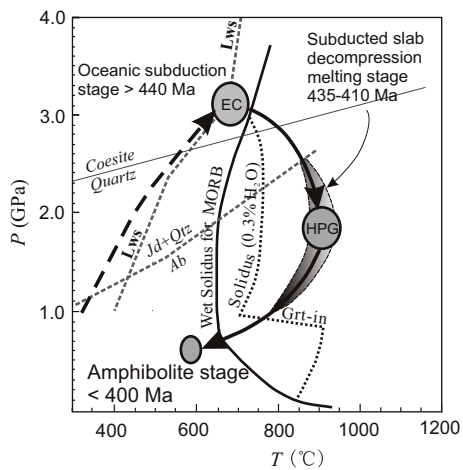


Fig. 10. P - T - t diagram illustrating the decompression partial melting of eclogite during exhumation. Hydral minerals such as lawsonite, zoisite and phengite will be dehydrated during exhumation with increasing temperature and decreasing pressure. Decompression melting would occur as omphacite breaks down in the abite stability field, forming the mafic granulite residue with low-Na Cpx and Ca-Mg rich garnet. HPG: high-pressure granulite; EC: eclogite. The wet solidus and the solidus with 0.3% H_2O (assemblage containing hydrous phases) for middle ocean ridge basalt (MORB) are after (Vielzeuf and Schmidt, 2001). The stability field of lawsonite (Lws) is after (Poli and Schmidt, 2002).

et al., 2011), the syn-collisional trondhjemite in the West Gneiss Region, Norway (Labrousse et al., 2011), and ~430 Ma adakite in the North Qilian orogen (Chen et al., 2012). Although the rock assemblage of this study shows some discrepancy with modern adakites, the tonalitic-trondhjemitic magma, especially the compositionally uniform tonalite pluton, are particularly relevant and important for understanding the petrogenesis of adakites associated with orogenesis.

In the Phanerozoic, continental collision zones (vs. active subduction zones) are argued to be primary sites for preserving juvenile crust and maintaining net continental crustal growth (Niu and O'Hara, 2009; Niu et al., 2013). In this Phanerozoic model, the juvenile crust is dominated by syncollisional granitoids without the “adakite signature” such as the voluminous batholiths along many orogenic belts on the greater Tibetan Plateau (see Mo et al., 2008; Niu et al., 2013). Our continental collision and exhumation model explored in this paper explains the origin of adakite and adakitic rocks unrelated to active subduction zones (e.g., the Present-day Pacific), but genetically associated with continental collision zones. More adakites are recognized in continental collision zones in recent years (see Chung et al., 2003, 2005). Given their dominantly mantle isotopic signatures, these adakites represent juvenile material and net contribution to crustal growth. The orogenic adakites will complement to the volumetrically significant “non-adakitic” batholiths for net continental crust growth (see Niu et al., 2013).

In this context, we hypothesize that the petrogenesis of adakites we report here in response to the orogenesis from seafloor subduction, ocean basin closing, continental

collision, subduction, exhumation and eclogite melting may be the very process for the petrogenesis of the Archean TTG. Although among all the syncollisional granitoids associated with a number of the collision zones on the Greater Tibetan Plateau that we have sampled are non-adakitic (see Niu et al., 2013), adakite intrusive are common and we are in the process of improving of hypothesis of “continental collisional zones as primary sites for net continental crust growth” (Niu et al., 2013), including incorporating adakitic rocks in the context syncollisional magmatism and continental crust growth.

ACKNOWLEDGEMENTS

We thank H.Q. Xie and D.Y. Liu for SHRIMP dating, C.F. Li for Sr-Nd isotopic analysis. We also thank Steve Foley and two anonymous reviewers for their constructive official review comments and smoothing the prose, which led to a better presentation of the final product. This study was supported by the National Natural Science Foundation of China (Grant Nos. 41372060, 40825007, 41121062, 41130314), Basic geological survey programs of China Geological Survey (1212011121258), and the Major State Basic Research Development Projects (2009CB825007).

REFERENCES

- Arculus R. J., Lapierre H. and Jaillard E. (1999) Geochemical window into subduction and accretion processes: Raspas metamorphic complex, Ecuador. *Geology* **27**, 547–550.
- Atherton M. P. and Petford N. (1993) Generation of sodium-rich magmas from newly underplated basaltic crust. *Nature* **362**, 144–146.
- Auzanneau E., Vielzeuf D. and Schmidt M. W. (2006) Experimental evidence of decompression melting during exhumation of subducted continental crust. *Contrib. Miner. Petrol.* **152**, 125–148.
- Beate B., Monzier M., Spikings R., Cotten J., Silva J., Bourdon E. and Eissen J.-P. (2001) Mio-Pliocene adakite generation related to flat subduction in southern Ecuador: the Quimsacocha volcanic center. *Earth Planet. Sci. Lett.* **192**, 561–570.
- Beaumont C., Jamieson R. A., Butler J. P. and Warren C. J. (2009) Crustal structure: a key constraint on the mechanism of ultra-high-pressure rock exhumation. *Earth Planet. Sci. Lett.* **287**, 116–129.
- Bromiley G. D. and Redfern S. A. T. (2008) The role of TiO_2 phases during melting of subduction-modified crust: Implications for deep mantle melting. *Earth Planet. Sci. Lett.* **267**, 301–308.
- Castillo P. (2006) An overview of adakite petrogenesis. *Chin. Sci. Bull.* **51**, 257–268.
- Castillo P. R. (2012) Adakite petrogenesis. *Lithos* **134–135**, 304–316.
- Castillo P. R., Janney P. E. and Solidum R. (1999) Petrology and geochemistry of Camiguin Island, southern Philippines: insights into the source of adakite and other lavas in a complex arc tectonic setting. *Contrib. Miner. Petrol.* **134**, 33–51.
- Chen Y. X., Xia X. H. and Song S. G. (2012) Petrogenesis of Aoyougou high-silica adakite in the North Qilian orogen, NW China: evidence for decompression melting of oceanic slab. *Chin. Sci. Bull.* **57**, 2289–2301.
- Chopin C. (2003) Ultrahigh-pressure metamorphism: tracing continental crust into the mantle. *Earth Planet. Sci. Lett.* **212**, 1–14.
- Chung S. L., Liu D. Y. and Ji J. Q. (2003) Adakites from continental collision zones: melting of thickened lower crust beneath southern Tibet. *Geology* **31**, 1021–1024.
- Chung S. L., Chu M. F., Zhang Y. Q., Xie Y. W., Lo C. H., Lee T. Y., Lan C. Y., Li X. H., Zhang Q. and Wang Y. Z. (2005) Tibetan tectonic evolution inferred from spatial and temporal variations in post-collisional magmatism. *Earth Sci. Rev.* **68**, 173–196.
- Clarke G. L., Daczko N. R. and Miescher D. (2013) Identifying Relic Igneous Garnet and Clinopyroxene in Eclogite and Granulite, Breaksea Orthogneiss. *New Zealand J. Petrol.* **54**, 1921–1938.
- Defant M. J. and Drummond M. S. (1990) Derivation of some modern arc magmas by melting of young subducted lithosphere. *Nature* **347**, 662–665.
- Dreher S. T., Macpherson C. G., Pearson D. G. and Davidson J. P. (2005) Re-Os isotope studies of Mindanao adakites: implications for sources of metals and melts. *Geology* **33**, 957–960.
- Eckert O. J., Newton R. C. and Kleppa O. J. (1991) The ΔH of reaction and recalibration of garnet-pyroxene-plagioclase-quartz geobarometers in the CMAS system by solution calorimetry. *Am. Mineral.* **76**, 148–160.
- Ellis D. J. and Green D. H. (1979) An experimental study of the effect of Caupon garnet-clinopyroxene Fe–Mg exchange equilibria. *Contrib. Miner. Petrol.* **71**, 13–22.
- Ernst W. G. (2001) Subduction, ultrahigh-pressure metamorphism, and regurgitation of buoyant crustal slices—implications for arcs and continental growth. *Phys. Earth Planet. Inter.* **127**, 253–275.
- Foley S., Barth M. and Jenner G. (2000) Rutile/melt partition coefficients for trace elements and an assessment of the influence of rutile on the trace element characteristics of subduction zone magmas. *Geochim. Cosmochim. Acta* **64**, 933–938.
- Foley S., Tiepolo M. and Vannucci R. (2002) Growth of early continental crust controlled by melting of amphibolite in subduction zones. *Nature* **417**, 837–840.
- Garrison J. M. and Davidson J. P. (2003) Dubious case for slab melting in the Northern volcanic zone of the Andes. *Geology* **31**, 565–568.
- Gerya T. (2011) Future directions in subduction modeling. *J. Geodyn.* **52**, 344–378.
- Green T. H. (1995) Significance of Nb/Ta as an indicator of geochemical processes in the crust-mantle system. *Chem. Geol.* **120**, 347–359.
- Green T. H. and Pearson N. J. (1986) Ti-rich accessory phase saturation in hydrous mafic-felsic compositions at high P, T. *Chem. Geol.* **54**, 185–201.
- Gutscher M.-A., Maury F., Eissen J.-P. and Bourdon E. (2000) Can slab melting be caused by flat subduction? *Geology* **28**, 535–538.
- Hacker B. R. and Peacock S. M. (1995) Creation, preservation, and exhumation of UHPM rocks. In *Ultrahigh Pressure Metamorphism* (eds. R. G. Coleman and X. Wang). Cambridge University Press, New York, pp. 159–181.
- Hermann J. and Spandler C. J. (2008) Sediment melts at sub-arc depths: an experimental study. *J. Petrol.* **49**, 717–740.
- Hermann J., Rubatto D., Korsakov A. and Shatsky V. S. (2001) Multiple zircon growth during fast exhumation of diamondiferous, deeply subducted continental crust (Kokchetav Massif, Kazakhstan). *Contrib. Miner. Petrol.* **141**, 66–82.
- Hu Z. C., Liu Y. S., Gao S., Liu W. G., Yang L., Zhang W., Tong X. R., Lin L., Zong K. Q., Li M., Chen H. H. and Zhou L. (2012) Improved in situ Hf isotope ratio analysis of zircon using newly designed X skimmer cone and Jet sample cone in combination with the addition of nitrogen by laser ablation

- multiple collector ICP-MS. *J. Anal. At. Spectrom.* **27**, 1391–1399.
- Kay R. W. (1978) Aleutian magnesian andesites: melts from subducted Pacific Ocean crust. *J. Volcanol. Geothermal. Res.* **4**, 117–132.
- Katayama I. and Nakashima S. (2003) Hydroxyl in clinopyroxene from the deep subducted crust: evidence for H₂O transport into the mantle. *Am. Mineral.* **88**, 229–234.
- Klemme S., Blundy J. D. and Wood B. J. (2002) Experimental constraints on major and trace element partitioning during partial melting of eclogite. *Geochim. Cosmochim. Acta* **66**(17), 3109–3123.
- Korsakov A. V. and Hermann J. (2006) Silicate and carbonate melt inclusions associated with diamonds in deeply subducted carbonate rocks. *Earth Planet. Sci. Lett.* **241**, 104–118.
- Kotkova J. and Harley S. L. (2010) Anatexis during high-pressure crustal metamorphism: Evidence from garnet-whole-rock REE relationships and zircon-rutile Ti-Zr thermometry in leucogranulites from the Bohemian Massif. *J. Petrol.* **51**, 1967–2001.
- Labrousse L., Jolivet L., Andersen T. B., Agard P., Hebert R., Maluski H. and Schärer U. (2004) Pressure-temperature-time deformation history of the exhumation of ultra-high pressure rocks in the Western Gneiss Region, Norway. *Geol. Soc. Am. Spec. Pap.* **380**, 155–183.
- Labrousse L., Prouteau G. and Ganzhorn A.-C. (2011) Continental exhumation triggered by partial melting at ultrahigh pressure. *Geology* **39**, 1171–1174.
- Lang H. M. and Gilotti J. A. (2007) Partial melting of metapelites at ultrahigh-pressure conditions, Greenland Caledonides. *J. Metamorph. Geol.* **25**(2), 129–147.
- Li Z. H., Xu Z. Q. and Gerya T. V. (2011) Flat versus steep subduction: contrasting modes for the formation and exhumation of high- to ultrahigh-pressure rocks in continental collision zones. *Earth Planet. Sci. Lett.* **301**, 65–77.
- Macpherson C. G., Dreher S. T. and Thirwall M. F. (2006) Adakites without slab melting: high pressure processing of basaltic island arc magma, Mindanao, the Philippines. *Earth Planet. Sci. Lett.* **243**, 581–593.
- Martin H., Smithies R. H., Rapp R., Moyen J.-F. and Champion D. (2005) An overview of adakite, tonalite-trondhjemite-granodiorite (TTG), and sanukitoid: relationships and some implications for crustal evolution. *Lithos* **79**, 1–24.
- Mattinson C. G., Wooden J. L., Liou J. G., Bird D. K. and Wu C. L. (2006) Age and duration of eclogite-facies metamorphism, North Qaidam HP/UHP terrane, western China. *Am. J. Sci.* **306**, 683–711.
- Mattinson C. G., Wooden J. L., Zhang J. and Bird D. K. (2009) Paragneiss zircon geochronology and trace element geochemistry, North Qaidam HP/UHP terrane, western China. *J. Asian Earth Sci.* **35**, 298–309.
- Mo X. X., Niu Y. L., Dong G. C., Zhao Z. D., Hou Z. Q., Zhou S. and Ke S. (2008) Contribution of syncollisional felsic magmatism to continental crust growth: A case study of the Paleogene Linzizong Volcanic Succession in southern Tibet. *Chem. Geol.* **250**, 49–67.
- Nehring F., Foley S. F., Hölttä P. and Van Den Kerkhof A. M. (2009) Internal differentiation of the archean continental crust: fluid-controlled partial melting of granulites and TTG–amphibolite associations in central Finland. *J. Petrol.* **50**, 3–35.
- Niu Y. L. (2004) Bulk-rock major and trace element compositions of abyssal peridotites: implications for mantle melting, melt extraction and post-melting processes beneath ocean ridges. *J. Petrol.* **45**, 2423–2458.
- Niu Y. L. and Batiza R. (1997) Trace element evidence from seamounts for recycled oceanic crust in the eastern equatorial Pacific mantle. *Earth Planet. Sci. Lett.* **148**, 471–484.
- Niu Y. L. and O'Hara M. J. (2009) MORB mantle hosts the missing Eu (Sr, Nb, Ta and Ti) in the continental crust: new perspectives on crustal growth, crust-mantle differentiation and chemical structure of oceanic upper mantle. *Lithos* **112**, 1–17.
- Niu Y. L., Zhao Z. D., Zhu D. C. and Mo X. X. (2013) Continental collision zones are primary sites for net continental crust growth – a testable hypothesis. *Earth-Sci. Rev.* **127**, 96–110.
- Parkinson C. D. and Kohn M. J. (2002) Continental subduction to depths of 200 km: implications for intra-continental ultrapotassic magmatism. In *The Diamond-Bearing Kokchetav Massif, Kazakhstan* (eds. C. D. Parkinson, I. Katayama, J. G. Liou and S. Maruyama). Universal Academy Press, Tokyo, Japan.
- Peacock S. M., Rushmer T. and Thompson A. B. (1994) Partial melting of subducting oceanic crust. *Earth Planet. Sci. Lett.* **121**, 227–244.
- Poli S. and Schmidt M. W. (2002) Petrology of subducted slabs. *Annu. Rev. Earth Planet. Sci.* **30**, 207–235.
- Powell R. (1985) Regression diagnostics and robust regression in geothermometer/geobarometer calibration: the garnet-clinopyroxene geothermometer revisited. *J. Metamorph. Geol.* **3**, 231–232.
- Rapp R. P., Shimizu N. and Norman M. D. (2003) Growth of early continental crust by partial melting of eclogite. *Nature* **425**, 605–609.
- Rudnick R. L. (1995) Making continental continental crust. *Nature* **378**, 571–578.
- Ryerson F. and Watson E. (1987) Rutile saturation in magmas: implications for Ti–Nb–Ta depletion in island-arc basalts. *Earth Planet. Sci. Lett.* **86**, 225–239.
- Sajona F. G., Maury R. C., Bellon H., Cotten J., Defant M. J. and Pubellier M. (1993) Initiation of subduction and the generation of slab melts in western and eastern Mindanao, Philippines. *Geology* **21**, 1007–1010.
- Schmidt M. W. and Poli S. (1998) Experimentally based water budgets for dehydrating slabs and consequences for arc magma generation. *Earth Planet. Sci. Lett.* **163**, 361–379.
- Skjerlie K. P. and Patiño Douce A. E. (2002) The fluid-absent partial melting of a zoisite-bearing quartz eclogite from 1.0 to 3.2 GPa: implications for melting in thickened continental crust and for subduction-zone processes. *J. Petrol.* **43**, 291–314.
- Song S. G., Yang J. S., Liou J. G., Wu C. L., Shi R. D. and Xu Z. Q. (2003a) Petrology, geochemistry and isotopic ages of eclogites from the Dulan UHPM Terrane, the North Qaidam, NW China. *Lithos* **70**, 195–211.
- Song S. G., Yang J. S., Xu Z. Q., Liou J. G. and Shi R. D. (2003b) Metamorphic evolution of the coesite-bearing ultrahigh-pressure terrane in the North Qaidam, Northern Tibet, NW China. *J. Metamorph. Geol.* **21**, 631–644.
- Song S. G., Zhang L. F., Chen J., Liou J. G. and Niu Y. L. (2005a) Sodic amphibole exsolutions in garnet from garnet-peridotite, North Qaidam UHPM belt, NW China: implications for ultradeep-origin and hydroxyl defects in mantle garnets. *Am. Mineral.* **90**, 814–820.
- Song S. G., Zhang L. F., Niu Y. L., Su L., Jian P. and Liu D. Y. (2005b) Geochronology of diamond-bearing zircons from garnet peridotite in the North Qaidam UHPM belt, Northern Tibetan Plateau: a record of complex histories from oceanic lithosphere subduction to continental collision. *Earth Planet. Sci. Lett.* **234**, 99–118.
- Song S. G., Zhang L. F., Niu Y. L., Su L., Song B. A. and Liu D. Y. (2006) Evolution from oceanic subduction to continental collision: a case study from the Northern Tibetan Plateau based on geochemical and geochronological data. *J. Petrol.* **47**, 435–455.
- Song S. G., Zhang L. F., Niu Y. L., Wie C. J., Liou J. G. and Shu G. M. (2007) Eclogite and carpholite-bearing metasedimentary

- rocks in the North Qilian suture zone, NW China: implications for early palaeozoic cold oceanic subduction and water transport into mantle. *J. Metamorph. Geol.* **25**, 547–563.
- Song S. G., Su L. and Niu Y. L. (2009) Generation of adakite: melting of eclogite during exhumation of UHPM terrane. *Geochim. Cosmochim. Acta* **73**, A1252.
- Song S. G., Su L., Li X.-H., Zhang G., Niu Y. L. and Zhang L. F. (2010) Tracing the 850-Ma continental flood basalts from a piece of subducted continental crust in the North Qaidam UHPM belt, NW China. *Precambr. Res.* **183**, 805–816.
- Song S. G., Su L., Li X.-H., Niu Y. L. and Zhang L. F. (2012) Grenville-age orogenesis in the Qaidam-Qilian block: the link between South China and Tarim. *Precambr. Res.* **220–221**, 9–22.
- Song S. G., Niu Y. L., Su L. and Xia X. H. (2013) Tectonics of the North Qilian orogen, NW China. *Gondwana Res.* **23**, 1378–1401.
- Song S. G., Niu Y. L., Su L., Zhang C. and Zhang L. F. (2014) Continental orogenesis from ocean subduction, continent collision/subduction, to orogen collapse, and orogen recycling: the example of the North Qaidam UHPM belt, NW China. *Earth Sci. Rev.* **129**, 59–84.
- Spandler C., Yaxley G., Green D. H. and Rosenthal A. (2008) Phase Relations and Melting of Anhydrous K-bearing Eclogite from 1200 to 1600 °C and 3 to 5 GPa. *J. Petrol.* **49**, 771–795.
- Sun, S. -S. and McDonough, W. F. (1989) Chemical and isotopic systematics of oceanic basalt: implications for mantle composition and processes. In: *Magmatism in the Ocean Basins*, vol. 42 (eds. A. D. Saunders and M. J. Norry). Geological Society of London, Special Publication. p. 313–345.
- Topuz G., Okay A. I., Altherr R., Schwarz W. H., Siebel W., Zack T., Satlr M. and Sen C. (2011) Post-collisional adakite-like magmatism in the Agvanis Massif and implications for the evolution of the Eocene magmatism in the Eastern Pontides (NE Turkey). *Lithos* **125**, 131–150.
- Vanderhaeghe O. and Teyssier C. (2001) Partial melting and flow of orogens. *Tectonophysics* **342**, 451–472.
- Vielzeuf D. and Schmidt M. W. (2001) Melting relations in hydrous systems revisited: application to metapelites, metagreywackes and metabasalts. *Contrib. Miner. Petrol.* **141**, 251–267.
- Wallis S., Tsuboi M., Suzuki K., Fanning M., Jiang L. and Tanaka T. (2005) Role of partial melting in the evolution of the Sulu (eastern China) ultrahigh-pressure terrane. *Geology* **33**, 129–132.
- Wei C. J. and Clarke G. L. (2011) Calculated phase equilibria for MORB compositions: a reappraisal of the metamorphic evolution of lawsonite eclogite. *J. Metamorph. Geol.* **29**, 939–952.
- Xiao Y. Y., Lavis S., Niu Y. L., Pearce J. A., Li H. K., Wang H. C. and Davidson J. (2012) Trace element transport during subduction-zone ultrahigh pressure metamorphism: evidence from Western Tianshan, China. *Geol. Soc. Am. Bull.* **124**, 1113–1129.
- Xiao Y. Y., Niu Y. L., Song S. G., Davidson J. and Liu X. M. (2013) Elemental responses to subduction-zone metamorphism: constraints from the North Qilian Mountain, NW China. *Lithos* **160**(161), 55–67.
- Xiong X.-L., Adam J. and Green T. (2005) Rutile stability and rutile/melt HFSE partitioning during partial melting of hydrous basalt: implications for TTG genesis. *Chem. Geol.* **218**, 339–359.
- Xiong X.-L. (2006) Trace element evidence for growth of early continental crust by melting of rutile-bearing hydrous eclogite. *Geology* **34**, 945–948.
- Xu H., Ye K., Song Y., Chen Y., Zhang J., Liu Q. and Guo S. (2013) Prograde metamorphism, decompressional partial melting and subsequent melt fractional crystallization in the Weihai migmatitic gneisses, Sulu UHP terrane, eastern China. *Chem. Geol.* **341**, 16–37.
- Xu J.-F., Shinjo R., Defant M. J., Wang Q. and Rapp R. P. (2002) Origin of Mesozoic adakitic intrusive rocks in the Ningzhen area of east China: partial melting of delaminated lower continental crust? *Geology* **30**, 1111–1114.
- Yang J. S., Wu C. L., Zhang J. X., Shi R. D., Meng F. C., Wooden J. and Yang H. Y. (2006) Protolith of eclogites in the north Qaidam and Altun UHP terrane, NW China: earlier oceanic crust? *J. Asian Earth Sci.* **28**, 185–204.
- Yang Y. H., Zhang H. F., Chu Z. Y., Xie L. W. and Wu F. Y. (2010) Combined chemical separation of Lu, Hf, Rb, Sr, Sm and Nd from a single rock digest and precise and accurate isotope determinations of Lu-Hf, Rb-Sr and Sm-Nd isotope systems using Multi-collector ICP-MS and TIMS. *Int. J. Mass Spectrom.* **290**, 120–126.
- Yogodzinski G. M., Lees J. M., Churikova T. G., Dorendorf F., Woerner G. and Volynets O. N. (2001) Geochemical evidence for the melting of subducting oceanic lithosphere at plate edges. *Nature* **409**, 500–504.
- Yu S., Zhang J. and Del Real P. G. (2012) Geochemistry and zircon U-Pb ages of adakitic rocks from the Dulan area of the North Qaidam UHP terrane, north Tibet: constraints on the timing and nature of regional tectonothermal events associated with collisional orogeny. *Gondwana Res.* **21**, 167–179.
- Zeng L., Gao L.-E., Xie K. and Liu-Zeng J. (2011) Mid-Eocene high Sr/Y granites in the Northern Himalayan Gneiss Domes: melting thickened lower continental crust. *Earth Planet. Sci. Lett.* **303**, 251–266.
- Zhang G. B., Song S. G., Zhang L. F. and Niu Y. L. (2008) The subducted oceanic crust within continental-type UHP metamorphic belt in the North Qaidam, NW China: evidence from petrology, geochemistry and geochronology. *Lithos* **104**, 99–108.
- Zhang G. B., Ellis D. J., Christy A. G., Zhang L. F., Niu Y. L. and Song S. G. (2009) UHP metamorphic evolution of coesite-bearing eclogite from the Yuka terrane, North Qaidam UHPM belt, NW China. *Eur. J. Mineral.* **21**, 1287–1300.
- Zhang J. X., Meng F. C. and Wan Y. S. (2007) A cold Early Palaeozoic subduction zone in the North Qilian Mountains, NW China: petrological and U-Pb geochronological constraints. *J. Metamorph. Geol.* **25**, 285–304.
- Zhang J. X., Mattinson C. G., Yu S. Y., Li J. P. and Meng F. C. (2010) U-Pb zircon geochronology of coesite-bearing eclogites from the southern Dulan area of the North Qaidam UHP terrane, northwestern China: spatially and temporally extensive UHP metamorphism during continental subduction. *J. Metamorph. Geol.* **28**, 955–978.
- Zhao Z.-F., Zheng Y.-F., Zhang J., Dai L.-Q., Li Q. and Liu X. (2012) Syn-exhumation magmatism during continental collision: evidence from alkaline intrusives of Triassic age in the Sulu orogen. *Chem. Geol.* **328**, 70–88.